Marine Chemistry 249 (2023) 104223

Contents lists available at ScienceDirect

Marine Chemistry

journal homepage: www.elsevier.com/locate/marchem

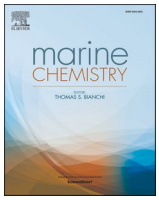

The biogeochemistry of zinc and cadmium in the Amundsen Sea, coastal Antarctica

Hung-An Tian [a,*], Mathijs van Manen [a], Flora Wille [a], Jinyoung Jung [b], SangHoon Lee [b], Tae-Wan Kim [b], Shigeru Aoki [c], Charlotte Eich [d,e], Corina P.D. Brussaard [d,e], Gert-Jan Reichart [a,f], Tim M. Conway [g], Rob Middag [a,h,*]

[a] NIOZ Royal Netherland Institute for Sea Research, Department of Ocean Systems, PO Box 59, 1790 AB Den Burg, the Netherlands
[b] Korea Polar Research Institute, 26, Songdomirae-ro, Yeonsu-gu, Incheon 21990, Republic of Korea
[c] Institute of Low Temperature Science, Hokkaido University, Sapporo 060-0819, Japan
[d] NIOZ Royal Netherland Institute for Sea Research, Department of Marine Microbiology and Biogeochemistry, PO Box 59, 1790 AB Den Burg, the Netherlands
[e] Institute for Biodiversity and Ecosystem Dynamics, Department of Freshwater and Marine Ecology, University of Amsterdam, 1090 GE Amsterdam, the Netherlands
[f] Department of Earth Sciences, Faculty of Geosciences, Utrecht University, 3584 CB Utrecht, the Netherlands
[g] College of Marine Science, University of South Florida, St Petersburg, FL 33701, USA
[h] Centre for Isotope Research - Oceans, University of Groningen, PO Box 72, 9700 AB Groningen, the Netherlands

ARTICLE INFO

Keywords:
GEOTRACES
Trace metals
Amundsen Sea Polynya
Biogeochemistry

ABSTRACT

The trace metals zinc (Zn) and cadmium (Cd) are both involved in the metabolic processes of marine phytoplankton, and as such, both metals play important roles in ocean biogeochemical cycles. In Antarctica, the Amundsen Sea (AS) experiences rapid ice shelf melting, and the Amundsen Sea polynya (ASP) hosts seasonal phytoplankton blooms in austral summer, with important implications for atmospheric carbon dioxide drawdown. However, the effects of ice melting and phytoplankton blooms on the biogeochemistry and distributions of Zn and Cd in the ASP remain poorly studied. Here, we present the first combined dataset of dissolved and particulate Zn and Cd in the AS (including the inflow and outflow to and from the Dotson and Getz ice shelves) collected as part of the GEOTRACES process study GPpr12. We use this dataset to assess the sources of both elements to the AS region and characterize the particle composition in the ASP. We find that the main source of both dissolved Zn and Cd in the AS is Circumpolar Deep Water (CDW), with an additional small flux of both metals from shelf sediments. By contrast, aerosol deposition, ice shelf melt, and sea ice melt are all deemed insignificant sources for either Zn or Cd in the AS. Labile particulate Zn and Cd dominate the total particulate pool in the surface layer, indicating that biological uptake is a predominant process for the cycling of both metals in the ASP, whereas sediment resuspension and ice shelf melt do not supply a significant amount of either particulate Zn or Cd. Additionally, we use two commonly used approaches to estimate biogenic and lithogenic particulate concentrations. We find high biogenic particulate concentrations at the surface, decreasing with depth, indicating remineralization plays an important role in the cycling of particulate metals. In contrast, lithogenic particulate metal concentrations remain low throughout the water column. We also show that the estimated uptake ratios of Zn and Cd relative to phosphate in the surface layer are lower than reported for the open Southern Ocean, likely related to the spatial and temporal variability of Fe in the AS. Overall, these new observations provide insight into the biogeochemistry of both Zn and Cd in the AS, a region that is subject to the influence of rapid climate change, which may have implications for the larger-scale cycling of trace metals in the Southern Ocean. Specifically, the amount of Zn and Cd supplied to the surface ASP will increase, given that the volume of CDW that flows towards the Dotson Ice Shelf is predicted to increase.

* Corresponding authors.
E-mail addresses: hatian1018@gmail.com (H.-A. Tian), rob.middag@nioz.nl (R. Middag).

https://doi.org/10.1016/j.marchem.2023.104223
Received 16 December 2021; Received in revised form 23 December 2022; Accepted 25 January 2023
Available online 30 January 2023

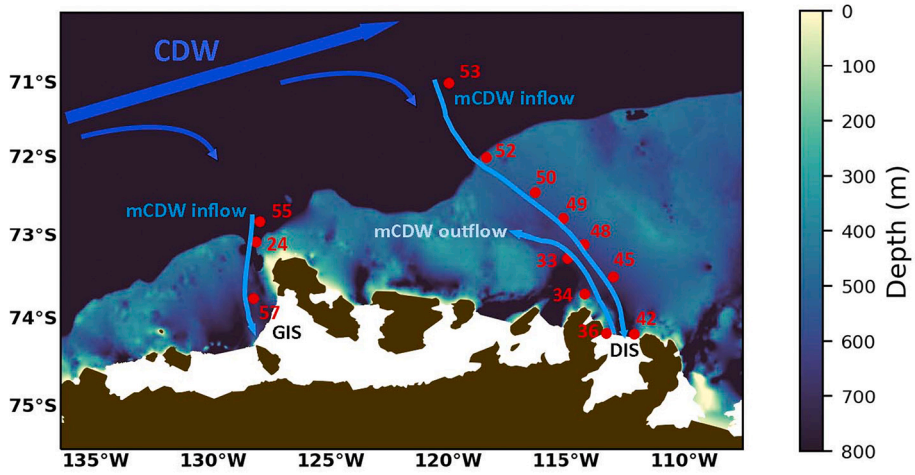

Fig. 1. GPpr12 Sampling stations in the Amundsen Sea. Two transects – Dotson transect (DIS) that includes 10 stations (Stns 53, 52, 50, 49, 48, 45, 42, 36, 34, and 33) and Getz transect (GIS) that includes 3 stations (Stns 55, 24, and 57). Approximate location of water mass flows are shown.

1. Introduction

Marine primary productivity is known to be regulated by the availability of sunlight, macronutrients (nitrate, phosphate, silicate), and micronutrients such as vitamin B_{12} and trace metals (e.g., iron (Fe), zinc (Zn), manganese (Mn), cobalt (Co), copper (Cu), and nickel (Ni), Croft et al., 2005; Morel et al., 2020; Twining and Baines, 2013). Among these bio-essential trace metals, Zn is involved in nearly 300 enzymes that are used in a range of processes in marine organisms (Vallee and Auld, 1990). For example, Zn is an essential component of both carbonic anhydrase (CA) and alkaline phosphatase (AP) enzymes which are responsible for the hydration/dehydration of carbon dioxide (CO_2) and the hydrolysis of phosphate esters, respectively (Morel et al., 1994). Similar to Zn, Cd may be involved in plankton metabolism, although Cd is not generally considered a bio-essential metal. For instance, Cd, together with Co, has been shown to be able to replace Zn in CA in the marine algae *Thalassiosira weissflogii* (Morel and Price, 2003; Sunda and Huntsman, 1995; Sunda and Huntsman, 1998), *Phaeodactylum tricornutum* and *Pseudonitzschia delicatissima* (Kellogg et al., 2020), as well as in *Emiliania huxleyi* (Saito et al., 2008; Sunda and Huntsman, 2000; Sunda and Huntsman, 2005; Xu and Morel, 2013), when ambient bioavailable Zn becomes depleted.

The distributions of both dissolved Zn and Cd in the ocean typically correlate well with macronutrients; the global distribution of Zn is more closely correlated to silicate (Si) than phosphate (PO_4) or nitrate (NO_3), with a concentration maximum at greater depth (e.g., Middag et al., 2019; Vance et al., 2017; Weber et al., 2018; Wyatt et al., 2014), whereas Cd is more closely correlated to PO_4 (e.g., Boyle et al., 1981; Bruland, 1980; Middag et al., 2018). Nevertheless, the relationship between either Zn and Si or Cd and PO_4 is not linear globally – changes in the steepness of the slopes in both global Zn:Si and Cd:PO_4 relationships (so-called 'kinks') are observed (e.g., Boyle, 1988; Cullen, 2006; de Baar et al., 1994; Middag et al., 2019; Middag et al., 2018). Such kinks are primarily driven by the advection and mixing of different water masses with various preformed Zn:Si and Cd:PO_4 ratios that are transported from high-latitude regions (e.g., the Southern Ocean) to low latitude oceans (e.g., Abouchami et al., 2014; Baars et al., 2014; de Souza et al., 2018; Middag et al., 2019; Middag et al., 2018; Sieber et al., 2019; Vance et al., 2017; Xie et al., 2015), underlining the fact that the distribution of macro/micronutrients and their elemental ratios in the global ocean are influenced by the waters from (and thus processes occurring in) the polar regions (e.g., Abouchami et al., 2014; Sieber et al., 2019; Sieber et al., 2020; Xie et al., 2015). Overall, the Southern Ocean is a hub of ocean circulation and a region of deep-water formation, playing a major role in redistributing elements through the global ocean. However, trace metal observations remain scarce in remote polar regions such as coastal Antarctica and the wider Southern Ocean.

Located adjacent to the Southern Ocean and West Antarctica, the Amundsen Sea (AS) is affected by the Southern Ocean circulation via Circumpolar Deep Water (CDW) (Fig. 1) (Jacobs et al., 1996; Kim et al., 2021; Kim et al., 2017; Miles et al., 2016; Thoma et al., 2008; Wåhlin et al., 2013), a relatively warm and saline water mass that blends with different deep-water masses, including North Atlantic Deep Water (NADW), Pacific Intermediate Water (PIW), Antarctic Bottom Water (AABW), and Antarctic Intermediate Water (AAIW). As CDW intrudes onto the continental shelves, it mixes with shelf waters and then becomes modified CDW (mCDW) (Arneborg et al., 2012). This mCDW flows underneath the ice shelves along the eastern flanks of deep troughs (inflow) (Assmann et al., 2013; Wåhlin et al., 2013), and subsequently leaves the ice shelves along the western flanks of these troughs (outflow) (Ha et al., 2014; Miles et al., 2016), which drives rapid melting of the Dotson Ice shelf (DIS) (Gourmelen et al., 2017), Pine Island Glacier (PIG) (Dutrieux et al., 2014; Jacobs et al., 1996; Jenkins et al., 2010), and Getz Ice Shelf (GIS) (Jacobs et al., 2012). Glaciers and ice shelves near the AS are observed to experience extremely fast thinning and collapsing (Rignot et al., 2008), and the AS is the primary area for accelerated melting of the West Antarctic Ice Sheet (WAIS). The melt of the WAIS is currently contributing to global sea level rise with an increasing rate (Shepherd et al., 2012). Such massive meltwater input has been attributed to an increasing extent of warm CDW intrusion onto Antarctic continental shelves (Jacobs et al., 2011; Jenkins et al., 2010; Shepherd et al., 2004). A change in the rate of flow of mCDW may also affect the cycling and distribution of ice shelf-derived materials, notably bio-essential elements, and thus could alter the biogeochemistry in the AS (Gerringa et al., 2012; Gerringa et al., 2020a; Henley et al., 2020; Miles et al., 2016; Planquette et al., 2013; Sherrell et al., 2015).

Melting of sea ice by seasonal warming and by upwelling of warm CDW, as well as by the offshore movement of sea ice by katabatic wind or currents, results in the formation of seasonal or year-round Antarctic coastal polynyas (Anderson, 1993; Arrigo and van Dijken, 2003; Pease, 1987), open areas surrounded by sea ice. In such polynyas, sunlight directly reaches surface waters, stimulating primary production (i.e., leading to phytoplankton blooms), but also allowing dramatic heat and air-sea exchange (Arrigo et al., 2012; Smith Jr and Comiso, 2008; Smith Jr and Gordon, 1997). Remarkably, the highest net primary production (NPP) recorded in the global ocean has been found in such coastal polynyas (Arrigo and van Dijken, 2003; Gerringa et al., 2012; Gerringa et al., 2020a; Mu et al., 2014). The phytoplankton blooms in Antarctic coastal polynyas thus promote considerable atmospheric CO_2 uptake. Specifically for the ASP bloom, the highest rate of annual NPP (per unit

area) (2.5 g C $m^{-2}y^{-2}$, Arrigo et al., 2012) among Antarctic polynyas has been observed, proposed to be fueled by external Fe inputs, which include the upwelling of relatively Fe-rich CDW (Gerringa et al., 2012; Gerringa et al., 2020a), melting of the DIS (Sherrell et al., 2015), melting of sea ice (Lannuzel et al., 2007; Sherrell et al., 2015), sedimentary diffusion, and sediment resuspension (Ardelan et al., 2010; Gerringa et al., 2012; Gerringa et al., 2020a; Sherrell et al., 2015).

To date, studies in the AS have suggested changes in elemental cycling that are also influencing local biological activity under scenarios of continued rapid climate change (e.g., Alderkamp et al., 2012; Alderkamp et al., 2015; Arrigo et al., 2012). However, although Zn and Cd can regulate rates of primary production and influence phytoplankton community composition (Bruland et al., 1991; Sunda and Huntsman, 2000; Twining and Baines, 2013), less attention has been given to Zn and Cd in the AS compared to Fe. To date, there has only been one dataset of dissolved Zn in the AS published (Sherrell et al., 2015), and there are no published data for dissolved Cd. Sherrell et al. (2015) speculated that sedimentary Zn input from the trough walls at the shelf break, together with Zn brought in by CDW, were both important sources of Zn to the AS. Furthermore, they concluded that strong biological removal in the surface layer and regeneration at depth was likely to be a dominant driver of the dissolved Zn distribution (Sherrell et al., 2015). Nevertheless, due to the limited amount of dissolved Zn data, a lack of Cd and particulate Zn data, and rapid changes in the region, we still have a limited understanding of the distributions and cycling of Zn and Cd, including the interaction between biological activity and these two metals.

In this study, to unravel the sources of both metals in the AS, we analyzed both dissolved and particulate Zn and Cd in samples collected using trace metal-clean procedures during Austral summer (December 2017 to February 2018) along transects that followed the main flow of mCDW (both inflow and outflow) in the AS (Fig. 1). Moreover, to investigate the particle composition and the metal uptake ratios, two particulate fractions – labile and refractory – were operationally separated for further discussion. These results provide the first investigation and a better understanding of the biogeochemistry of these bioactive dissolved and particulate metals (Zn and Cd) in the AS.

2. Materials and methods

2.1. Sampling region and sampling methods

During Austral Summer 2017/2018 (December 2017 to February 2018), seawater samples and suspended particles were collected cleanly along two water column transects in the AS (Fig. 1) from the Korean icebreaker R/V Araon during a GEOTRACES process study (GPpr12; expedition ANA08B). The first transect followed CDW that intruded from the open SO onto the Antarctic continental shelf via a subglacial trough, with CDW then becoming mCDW that flows south-eastward towards and underneath the DIS and subsequently leaves the DIS flowing north-westward (Fig. 1). The mCDW inflow and outflow were verified by shipboard measurement of current velocity and regular CTD data onboard the R/V Araon (Kim et al., 2021). Here, we refer to this first transect as the 'Dotson transect' that includes an open ocean station (Stn 53), a shelf break station (Stn 52), mCDW inflow stations (Stns 50, 49, 48, 45, 42), and mCDW outflow stations (Stns 36, 34, 33). The second transect followed CDW that flowed south-westward towards the GIS from the open ocean (Fig. 1). Here, we refer to this second transect as the 'Getz transect' that includes an off-shelf station (Stn 55), a shelf break station (Stn 24), and a shelf station (Stn 57). Each station comprised 10–14 sampling depths from the near-surface (~10 m) to 1000 m, or to 10–20 m above the seafloor for the stations shallower than 1000 m. However, we note that samples below 200 m at Stn 36 (part of the mCDW outflow) were not successfully collected due to a malfunctioning of the sampling system and therefore no metal data (and corresponding CTD and oxygen isotope data) are shown for this part of the water column.

Both dissolved and particulate samples from a total of 13 stations were collected using the Royal Netherlands Institute for Sea Research (NIOZ) "Titan" ultra clean sampling system for trace metals (de Baar et al., 2008). This system is made of titanium and equipped with high-purity, light-proof polypropylene (PP) samplers (modified from Rijkenberg et al., 2015). The sampling system was deployed on a 11 mm Dyneema cable without internal conducting wires and an SBE 17 plus V2 Searam in a titanium housing provided power, saved the CTD data, and closed the sampling bottles (23*L*) at pre-programmed depths. After recovery, the "Titan" sampling system was immediately transported into a clean, positive-pressure sampling container (temperature close to the ambient water temperature) where subsampling was conducted.

Dissolved seawater samples were filtered (0.2 μm filter cartridge, Sartorius, Sartobran-300, precleaned with sample seawater) into 125 mL Nalgene LDPE bottles (precleaned following GEOTRACES protocols, as described in Middag et al., 2019) under 0.5 bar of prefiltered nitrogen gas. The filtered samples were then acidified to 0.024 M HCl using 12 M ultrapure concentrated HCl (Baseline, Seastar Chemicals Inc), resulting in a final pH of ~1.8. Acidified samples were stored at room temperature for over 5 months before measurement of the concentrations back on shore at NIOZ. For particulate samples, unfiltered seawater (6–8 L) was subsampled as soon as the Titan system entered the sampling container, and the seawater was stored in acid-cleaned LDPE carboys that were covered by dark plastic bags until the moment of filtration (<3 h) close to the in-situ water temperature (Rauschenberg and Twining, 2015; Planquette and Sherrell, 2012). Before filtration, polyethersulfone (PES) disc filters (25 mm, 0.45 μm Pall Supor) were placed on polypropylene filter holders (Advantec) with polypropylene luer-locks (Cole-Palmer) that were attached to the carboy caps. Filters and filter holders were acid-cleaned beforehand with 3 times sub-boiled distilled 1.2 M HCl (VWR Chemicals – AnalaR NORMAPUR) at 60 °C for 24 h, then rinsed with ultrapure water (MQ, <18.2 MΩ-cm) water 5 times and eventually stored in ultrapure water before use following Ohnemus et al. (2014). Subsequently, carboys were mounted upside down, hanging from the Titan frame and connected to filtered nitrogen gas (0.3 bar overpressure). The volumes of filtration ranged from 0.25 L (surface samples) to 8 L (deep ocean samples), with a maximum duration of filtration of 2 h (GEOTRACES cookbook 2017). Eventually, the PES filters were folded in half and stored in acid-cleaned vials (Eppendorf) at −20 °C before analysis at NIOZ.

2.2. Sample processing and analysis

2.2.1. Ancillary parameters (salinity, temperature, depth, fluorescence, and nutrients)

For supporting ancillary parameters, a calibrated CTD (Seabird SBE 911+) with auxiliary sensors was mounted on the Titan sampling system to measure salinity (conductivity), temperature, depth (pressure), and fluorescence. Unfiltered seawater samples (~50 mL) were collected for inorganic nutrient analysis, including phosphate (PO_4) and silicate ($Si(OH)_4$). Inorganic nutrients were measured during the cruise using a four-channel Auto-Analyzer (QuAATRo, Seal Analytical, Germany), according to the Joint Global Ocean Flux Study (JGOFS) protocols described by Gordon et al. (2001). Precision on PO_4 and $Si(OH)_4$ measurements was ±0.02 and ± 0.28 μmol kg^{-1}, respectively (Jeon et al., 2021).

2.2.2. Phytoplankton pigment composition analysis

At one depth per station in the upper few tens of meters at selected stations (Stns 33, 34, 36, 42, 45, 49, 55, 24, and 57), samples were taken for pigment-based phytoplankton taxonomic composition analysis. Seawater samples were filtered at 1 °C through a GF/F glass fiber filter (45 mm diameter; Whatman, Cytiva, Marlborough, USA), using a vacuum pump (Pall, Port Washington, NY, USA) set at 200 mbar. The average sample volume that was needed to display a green colour on the

filter (indicating sufficient material for analysis) was 1.7 L (ranging from 0.75 to 2.7 L). Filters were double-wrapped in aluminum foil, snap-frozen in liquid nitrogen, and stored at −80 °C until analysis. For analysis, the filters were freeze-dried, and pigments were dissolved in acetone (van Leeuwe et al., 2006). A Zorbax Eclipse XDB-C8 column (3.5 μm particle size) was used for High-Performance Liquid Chromatography (HPLC) pigment separation (Van Heukelem and Thomas, 2001). Detection based on retention time and diode array spectroscopy (Waters 996) at 436 nm was used. Most pigments were quantified manually using standards (DHI LAB products). The taxonomic composition of the phytoplankton (expressed as % of total chlorophyll *a* concentration) was determined using CHEMTAX (version 1.95, Mackey et al., 1996) as described by Selz et al. (2018). The starting ratios used for analysis have previously been used for Antarctic shelf regions (Selz et al., 2018). The endmember pigment compositions are re-defined and reported by Eich et al. (2022).

2.2.3. $\delta^{18}O$ analysis

We express the stable oxygen isotope ratio of a water sample as $\delta^{18}O$ with respect to Vienna Standard Mean Ocean Water (VSMOW). Water samples for $\delta^{18}O$ were drawn from the Niskin bottles mounted on the regular CTD rosette of the R/V Araon, which was deployed at the same stations as the Titan system, which was deployed at the same stations. Water from matching depths was collected by gravity filtration through inline pre-combusted filters held in acid-cleaned polycarbonate filter holders. A 30 mL glass vial with polypropylene cap and polypropylene-coated insert was used to collect the water sample. The glass vial was sealed with Parafilm and stored in refrigerators at 4 °C until analysis.

The $\delta^{18}O$ samples were processed using Finnigan DELTA plus and Elementar Isoprime Precision mass spectrometers at ILTS laboratory, Hokkaido University, Japan. The DELTA plus was coupled with an equilibration system, automatically shaking for about 8 h in an 18 °C water bath to equilibrate with CO_2, while the Isoprime Precision was coupled with an equilibration system consisting of a metal insulator set up for about 16 h at 30 °C. The precision of the analysis was estimated to be 0.02‰ based on duplicated measurements (Nakamura et al., 2014).

2.2.4. Dissolved metal sample processing

Back on shore, in the NIOZ clean laboratory (ISO class 7, ISO class 5 in working hoods), dissolved Zn (dZn) and dissolved Cd (dCd) were extracted and preconcentrated from acidified filtered seawater samples using a commercially available seawater preconcentration system (seaFAST-pico, ESI). The SeaFAST-pico preconcentration procedure that was used followed Gerringa et al. (2020b).

2.2.5. Particulate metal sample processing

As described by van Manen et al., 2022, particulate samples were operationally divided into two fractions – a labile particulate metal phase (LpMe) including Zn (LpZn) and Cd (LpCd), defined based on Berger et al. (2008) and as modified by Rauschenberg and Twining (2015), and a refractory particulate metal phase (RpMe) including Zn (RpZn) and Cd (RpCd), defined based on Planquette and Sherrell (2012). For LpMe, briefly, 1.8 mL of a solution of 4.35 M acetic acid (double distilled from VWR NORMAPUR by PFA Savillex Stills) and 0.02 M hydroxylamine hydrochloride (Sigma-Aldrich, 99.999% trace metal basis) was added to an Eppendorf vial (containing PES filters). The vials were then heated at 95 °C in a water bath for 10 min and subsequently allowed to cool to room temperature. Once the total contact time of the samples and leach solution reached 2 h, the filters were removed and placed into 30 mL perfluoroalkoxy beakers (PFA, Savillex) to facilitate further RpMe digestion. The remaining leachates were centrifuged at 16000 Relative Centrifugal Force (RCF) for 10 min. Subsequently, without disturbing the remaining particles, 1.6 mL of the solution was transferred to another PFA Teflon beaker and 100 μL of concentrated HNO_3 (AnalaR NORMAPUR, 2 times Savillex distillation) was added. This mixture was subsequently dried down at 110 °C. Once dried, the samples were re-dissolved in 2 mL 1.5 M HNO_3 with 10 ng mL^{-1} Rh as internal standard and refluxed again at 110 °C for 30 min. This final fraction was ready for ICP-MS analysis and was considered to contain LpMe.

For RpMe, the solution and particles that remained after centrifugation in the were placed in the same PFA beakers in which the filters removed from the Eppendorf vials were placed, and a solution 2 mL 8 M HNO_3 and 2.9 M HF (Supelco, Ultrapur 48%) was added. The samples were refluxed capped at 110 °C for 4 h. Afterwards, the solutions were transferred into a second set of PFA beakers, and the filter remained in the original vial. Ultrapure water (MQ, 18.2 MΩ-cm) was used to rinse the remaining filters in the original beakers, and the rinsing solution was transferred into the second PFA beakers with the samples. These samples were then dried down at 110 °C. Subsequently, samples were re-dissolved and refluxed with 1 mL of solution of 8 M HNO_3 and 15% H_2O_2 at 110 °C for 1 h, and dried down again at 110 °C afterwards. Finally, a solution of 2 mL 1.5 M HNO_3 with 10 ng mL^{-1} Rh was added to samples and refluxed at 110 °C for 30 min to re-dissolve. This final fraction was ready for ICP-MS analysis and was considered RpMe. Given that the solution remaining after the LpMe leaching procedure (0.2 mL) contains a small portion of the LpMe fraction, a correction was applied to RpMe to account for this (see Section 2.3.1.2). The sum of LpMe and RpMe is defined as total particulate metal (TpMe, labile + refractory).

Table 1
Procedural blanks, and dissolved Zn and Cd concentrations measured in reference seawater (SAFe D1 and GSC). SAFe D1 seawater was collected from 1000 m depth in the North Pacific Ocean during the Sampling and Analysis of Fe program (2004); GSC seawater was collected at 2 m at the North Pacific Ocean (coastal Santa Barbara Channel, 2009). Consensus values for these reference materials are shown, reproduced from GEOTRACES (https://www.geotraces.org/). Both selected reference seawaters were measured in one analytical session. All units are in nmol L^{-1} (mean ± 1 SD), converted from nmol kg^{-1} to nmol L^{-1} by using average seawater density (1.025 g/cm^{-3}). Limit of detection for dissolved Zn (0.03 nmol L^{-1}) is 3 times standard deviation of the procedural blank, whereas for Cd, in order to take Mo interference on Cd measurement into account, the limit of detection for dissolved Cd (0.003 nmol L^{-1}) is calculated from the standard deviation (3 times) of our in-house low metal concentration seawater (0.012 ± 0.001 nmol L^{-1}).

Dissolved metal (nmol L^{-1})		Blank	SAFe D1 (n = 3)	GSC (n = 3)
Zn	this study	0.02 ± 0.01	7.81 ± 0.04	1.34 ± 0.01
	consensus value	n/a	7.59 ± 0.35	1.43 ± 0.10
Cd	this study	0.002 ± 0.001	1.01 ± 0.01	0.35 ± 0.01
	consensus value	n/a	1.02 ± 0.03	0.36 ± 0.02

2.3. Trace metal concentration measurements

All samples were analyzed for trace metal concentrations using Inductively Coupled Plasma Mass Spectrometry (ICP-MS) on a Thermo Scientific Sector Field High Resolution Element 2 at NIOZ. A microFAST introduction system (ESI, USA) equipped with a PFA nebulizer with a sample introduction rate of 55 μL min^{-1} was used. The analytical procedure for ICP-MS measurements for dissolved and particulate metals are similar, based on Gerringa et al. (2020b). For the dissolved samples, an average of concentration of triplicate measurements (performed in three different analytical runs) was calculated. Sample concentrations were calibrated by a suite of calibrations during each analytical run, prepared by adding a mixed stock solution of multiple standards to both low-metal seawater and 1.5 M HNO_3; the former was preconcentrated in the same way as samples through the seaFAST-pico and used to quantify the concentration of dissolved samples, while the latter was used to monitor the recovery of the seaFAST-pico on a daily basis (after Biller and Bruland (2012). For particulate metals, a calibration was prepared based on standard additions to the same 1.5 M HNO_3 as used for particulate samples.

Table 2
Procedural blanks for particulate analysis, and particulate P, Al, Zn, and Cd concentrations (and recovery) measured for selected certified reference materials (BCR-414 and PACS-2). BCR-414 is a reference standard (plankton) certified by BCR (Community Bureau of Reference, the former reference materials programme of the European Commission), details can be found on the website of European Commission's Joint Research Centre (JRC, https://ec.europa.eu/info/departments/joint-research-centre_en). PACS-2 is a reference standard (marine sediment) collected and certified by the National Research Council of Canada (NRC, https://nrc.canada.ca/en). Units are a: nmol filter^{-1}; b: pmol filter^{-1}; c: μg g^{-1}; d: ng g^{-1}; e: mg g^{-1}.

Particulate metal (mean ± 1SD)		Blank (n = 9)			BCR-414 (n = 6)	PACS-2 (n = 3)
		labile	refractory	total		
Zn	This study	0.22[a] ± 0.08	0.04[a] ± 0.02	0.26[a] ± 0.09	107[c] ± 3	400[c] ± 56
	Certified value	n/a	n/a	n/a	112[c] ± 3	364[c] ± 3
	Recovery (%)	n/a	n/a	n/a	95 ± 2	110 ± 15
Cd	This study	0.13[b] ± 0.04	0.05[b] ± 0.05	0.19[b] ± 0.08	355[d] ± 10	2248[d] ± 184
	Certified value	n/a	n/a	n/a	383[d] ± 14	2110[d] ± 150
	Recovery (%)	n/a	n/a	n/a	93 ± 3	107 ± 9
Al	This study	0.36[a] ± 0.15	0.37[a] ± 0.21	0.73[a] ± 0.33	n/a	74[e] ± 7
	Certified value	n/a	n/a	n/a	n/a	66[e] ± 3.2
	Recovery (%)	n/a	n/a	n/a	n/a	113 ± 11
P	This study	0.09[a] ± 0.08	0.15[a] ± 0.21	0.24[a] ± 0.09	n/a	966[c] ± 99
	Certified value	n/a	n/a	n/a	n/a	960[c] ± 40
	Recovery (%)	n/a	n/a	n/a	n/a	101 ± 10

2.3.1. Blank, precision, and accuracy of ICP-MS measurement

2.3.1.1. Dissolved metals. The procedural blank for dissolved Zn and Cd ($n = 9$) were established at NIOZ by analyzing acidified MQ (pH ~1.8) processed using the same procedure as for real samples (Table 1). Blank values were the equivalent of <2% of real samples (Table 1). The precision and accuracy of measurements were evaluated by analysis of GEOTRACES SAFe ($n = 3$, SAFe D1, Johnson et al., 2007) and GSC (n = 3, GEOTRACES coastal surface seawater, 2009) reference materials, which were treated identically to dissolved samples. Measurements of both reference seawaters in this study were within the community consensus range (Table 1).

2.3.1.2. Particulate metals. For particulate metals, the procedural blank (n = 9) was evaluated using a blank filter that had not been in contact with seawater, processed through the leach and digestion procedure as done for real samples. The relative size of the procedural blank varied; for aluminum (Al), phosphorus (P), and Cd, the blank was the equivalent of <2% of the average concentrations of total particulate samples, whereas for Zn the procedural blank corresponded to ~20% of the average sample concentration. However, the blank values in this study were of the same order of magnitude as the blank values found by previous studies (Table 2) (Ohnemus et al., 2014; Rauschenberg and Twining, 2015). To assess the accuracy of the analysis of particulate metals, two certified reference materials (CRMs) – BCR-414 (freshwater phytoplankton, European Commission's Joint Research Centre) and PACS-2 (marine sediments, National Research Council of Canada), were processed and measured identically to the particulate filter samples (filters included). The recovery of target elements (Zn, Cd, Al, and P) from both CRMs was 93–113% (Table 2). In assessing uncertainty on particulate measurements, it should be noted that [RpCd] is significantly lower than [LpCd] (20–50 times lower). Further, given that [RpCd] is corrected for carry-over from the labile leach (0.2 mL of the solution from the labile leach ends up in the refractory fraction), this correction adds additional uncertainty to the refractory fraction; for example, if we assume 5% uncertainty for the labile leach measurement, the correction adds an additional uncertainty of ~9% if there is a factor of 20 difference between lable and refractory concentrations, and an additional ~28% if the difference in concentrations is a factor of 50.

3. Results

3.1. Hydrographic conditions

3.1.1. Water masses

The water column of the AS during our study comprised the three major water masses that are typically observed in the AS (Randall-Goodwin et al., 2015; Yager et al., 2012): Antarctic Surface Water (AASW), Winter Water (WW), and CDW that becomes mCDW on the continental shelf due to the mixing of CDW with overlying water (Fig. 2a). Located at the surface, AASW is relatively warm and fresh (Fig. 2a, Θ ~ −0.6 to −0.7 °C, S < 33.8), a result of enhanced solar irradiation in summer and associated sea ice melt. Along the Dotson transect, AASW is observed in the upper 40 m at mCDW inflow stations (Stns 50, 49, 48, and 45) and mCDW outflow stations (Stns 34 and 33) (Fig. 3a and b). In contrast, AASW was not clearly observed in the surface along the Getz transect (Fig. 3d and c). Underlying AASW, remnant WW from the winter season is colder and more saline (Fig. 2a, Θ ~ −1.7 to −1.8 °C, S: 34.3–34.4) due to brine rejection during sea ice formation, as well as the cooling of surface water during the cold season. Underlying WW, CDW consists of warmer and more saline water (Fig. 2a, Θ >1 °C, S > 34.7). Due to the mixing with overlying WW and melt water from the ice shelf, the potential temperature (referred to temperature hereafter) and salinity of CDW is diluted along the transects (Fig. 3). Relatively high temperatures were observed at 500 m at the mCDW inflow stations (Stns 45 and 42) and below 200 m at the mCDW outflow stations (Stns 36 and 34) (Fig. 3a and b), identifying the core of mCDW inflow and mCDW outflow, respectively.

3.1.2. Freshwater input ($\delta^{18}O$)

The size of the ASP changes during Antarctic summer due to seasonal melting and wind-driven transport of surrounding sea ice. To assess the change of sea ice coverage in the ASP during our sampling period, satellite data with 0.05° × 0.05° resolution from the Operational Sea Surface Temperature and Ice Analysis (OSTIA) system was used. At the beginning of the sampling period (23-01-2018) (Fig. 4a), the ASP was enclosed, gradually opening to the open ocean by the end of the sampling period (02-02-2018) (Fig. 4b). Along the Dotson transect, 6 stations (Stns 33, 34, 36, 42, 45, and 48) were in the ASP during the entire sampling period, whereas the other 4 stations (Stns 49, 50, 53, and 53) were either on the edge of the sea ice or covered by sea ice. Along the Getz transect, Stns 24 and 55 were covered by sea ice during the sampling period, whereas Stn 57 was on the edge of the sea ice at the beginning and then became ice free during the sampling period.

To further assess freshwater input into the ASP during the sampling period, measurements of oxygen isotopes ($\delta^{18}O$) and salinity of seawater were utilized to differentiate between sea ice melt, meteoric input, and CDW, all of which were quantified in a three end-member mass balance approach after Östlund and Hut (1984) and Meredith et al. (2013). Following Randall-Goodwin et al. (2015), we assigned three different endmembers in the AS, based on salinity and $\delta^{18}O$. A mass balance was calculated utilizing three equations:

$$f_{sim} + f_{met} + f_{CDW} = 1 \quad (1)$$

$$f_{sim} \times S_{sim} + f_{met} \times S_{met} + f_{CDW} \times S_{CDW} = S_{obs} \quad (2)$$

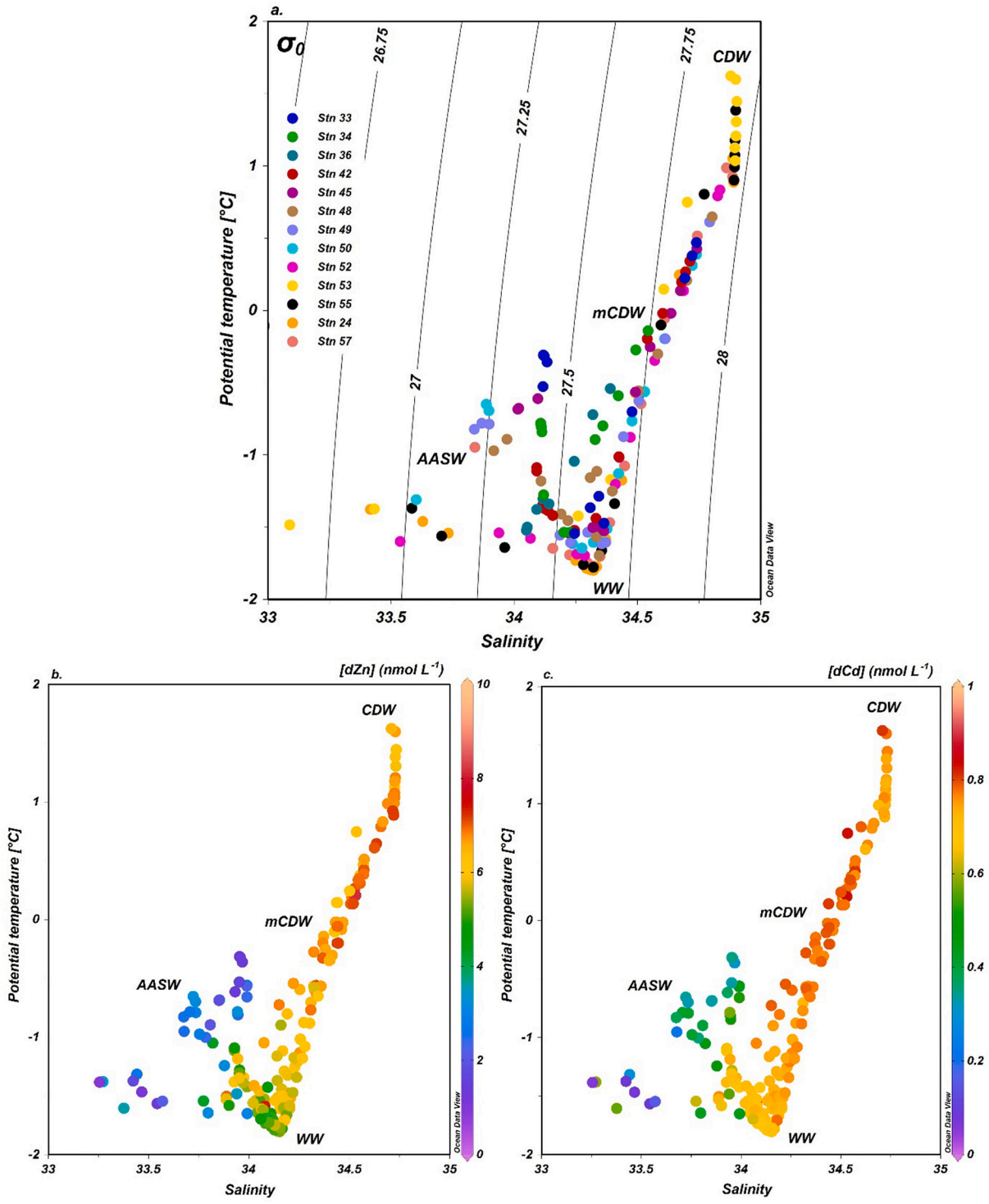

Fig. 2. Potential temperature (°C), salinity, [dZn] and [dCd] (nmol L^{-1}) plotted against salinity for all GPpr12 stations. a. Θ-S diagram, three water masses are identified: Antarctic Surface Water (AASW), Winter Water (WW), and Circumpolar Deep Water (CDW). b. [dZn] on Θ-S diagram. c. [dCd] on Θ-S diagram. Θ was derived using ODV version 5.3.0 (Schlitzer, 2020).

$$f_{sim} \times \delta_{sim} + f_{met} \times \delta_{met} + f_{CDW} \times \delta_{CDW} = \delta_{obs} \quad (3)$$

Here, *sim*, *met*, *CDW*, and *obs*, denote sea ice melt, meteoric water, circumpolar deep water, and observed values, respectively, and *f*, *S*, and *δ*, represent fraction, salinity, and $\delta^{18}O$, respectively. S_{sim}, S_{met}, S_{CDW}, δ_{sim}, δ_{met}, δ_{CDW}, are required to be constrained to obtain the contributions of each fraction (f_{sim}, f_{met}, f_{CDW}). Following Randall-Goodwin et al. (2015), we assign 7, 0 and 34.62, as the salinity of S_{sim}, S_{met}, and S_{CDW}, respectively, and 2.1‰, −25‰, and − 0.059‰ as the $\delta^{18}O$ endmember values for δ_{sim}, δ_{met}, and δ_{CDW}, respectively. The observed salinity in CDW at some stations appears higher than the endmember as used by Randall-Goodwin. et al. (2015), but as noted by those authors, salinity endmembers are likely to vary both seasonally and annually. The discrepancy that arises in our calculations from using either the CDW endmember from Randall-Goodwin. et al. (2015) (S: 34.62; $\delta^{18}O$: −0.059) or an CDW endmember definition based on our observations (S:

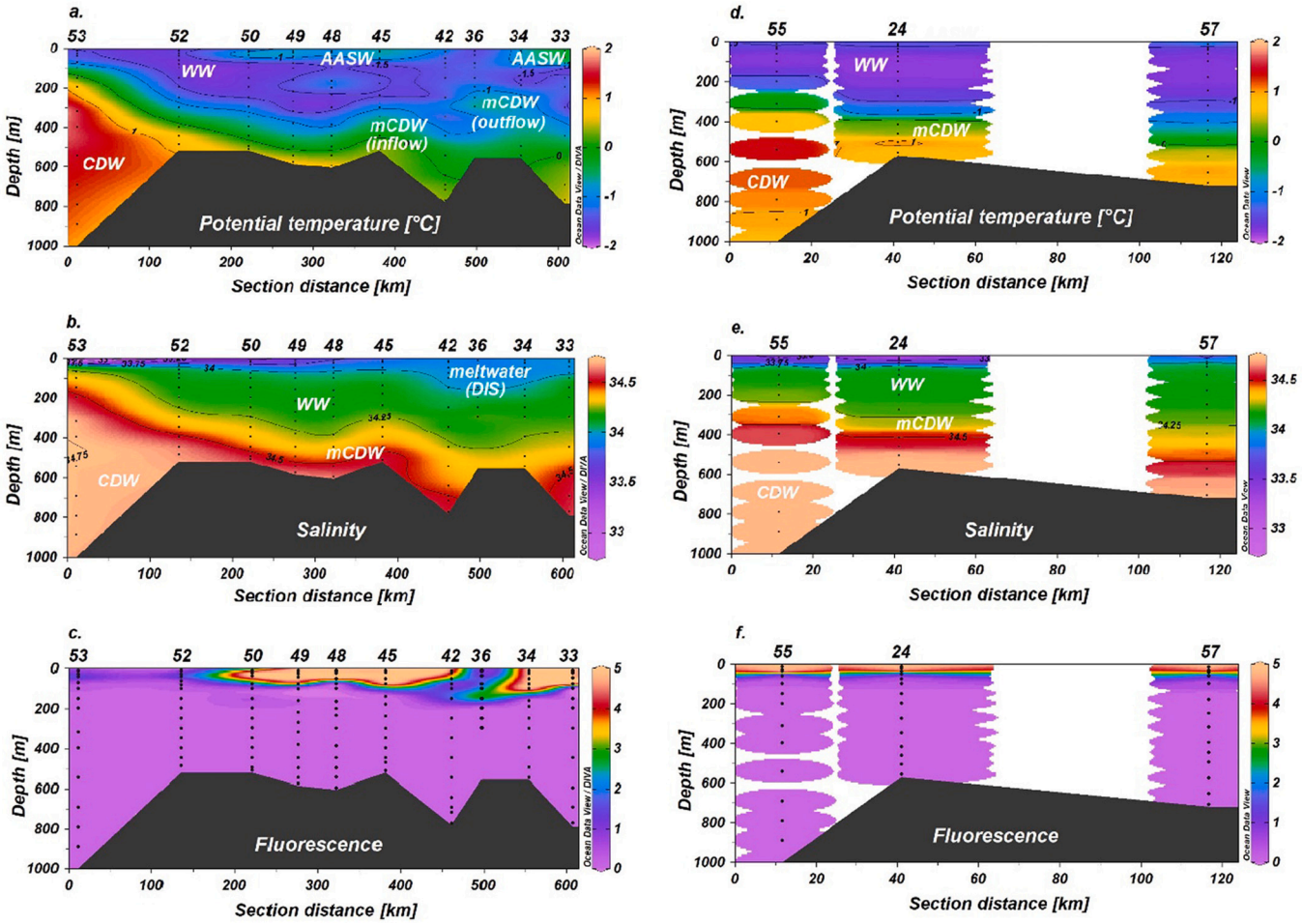

Fig. 3. Section plots of ancilliary hydrographic parameters along both transects of GPpr12. Dotson: a. potential temperature (°C), b. salinity, and c. fluorescence; Getz: d. potential temperature (°C), e. salinity, and f. fluorescence. It is noted that in Fig. 3a there is an artefact below 300 m at Stn 36 due to a malfunction of sampling bottles and therefore no data is shown for this depth interval.

34.71; $\delta^{18}O$: −0.04) is negligible (0.2% on f_{sim}, 0.09% on f_{met}, and 0.3% on f_{CDW}). Therefore, for consistency and comparison to previous studies, we use the same endmembers as defined by Randall-Goodwin et al. (2015). The results of this calculation show the extent of melting of sea ice/ice shelves and the distribution of CDW (Fig. 5). It should be noted the CDW endmember represents inflowing seawater that gets modified by the processes of sea ice melt and formation and meteoric water input that contribute to formation of AASW and WW. Thus, AASW and WW are not further distinguished in this model.

Relatively elevated f_{sim} (1–3%) was observed in the upper 40 m along both transects, specifically at the open ocean station (Stn 53), the shelf break station (Stn 52), and mCDW inflow stations (Stns 50 and 49) along the Dotson transect (Fig. 5b), and the off-shelf station (Stn 55), and the shelf break station (Stn 24) along the Getz transect (Fig. 5e). This result corresponds with the observations of the changing sea ice cover during the sampling period; the stations with elevated f_{sim} (Stns 53, 52, 50, 49, 55, and 24) were located either within the sea ice or on the edge of the sea ice (Fig. 4). Secondly, along the Dotson transect, elevated f_{met} (>2.5%) was observed in the upper 145 m at the mCDW inflow station (Stn 42) and mCDW outflow stations (Stns 36, 34, and 33) (Fig. 5c), indicating surface meltwater input from the ice shelf in the surface, consistent with the distribution of salinity (Fig. 3b). Along the Getz transect, comparatively smaller f_{met} (2–2.5%) than along the Dotson transect was observed in the upper 245 m of the shelf station (Stn 57) and the maximum depth extent of f_{met} gradually decreased offshore (Fig. 5f).

3.2. Phytoplankton

Along the Dotson transect, chlorophyll *a* (Chl a) autofluorescence was relatively elevated in the upper 100 m of most stations (Fig. 3c, Stns 33, 34, 36, 42, 45, 48, 49, and 50). At the shelf break station (Stn 52) and the open ocean station (Stn 53), fluorescence had a maximum at a shallower depth compared to the other stations (Fig. 3c). Along the Getz transect (Stns 55, 24, and 57), elevated fluorescence occurred over a shallower depth range (upper 40 m) at all three stations (Fig. 3f) than the Dotson transect. Here, we refer to the water column between the surface and the depth where maximum fluorescence was observed as the 'surface layer'. Below this surface maximum, the fluorescence signal rapidly declined. The stations with elevated fluorescence in the surface layer (relative to other stations) along the Dotson transect (Stns 33, 34, 36, 42, 45, 48, 49, and 50) and Getz transect (Stn 55, 24, and 57) are referred as phytoplankton bloom stations in the following sections as they have high Chl a standing stock and it is well established there is an annual phytoplankton bloom in the ASP (Alderkamp et al., 2015; Arrigo et al., 2012; Gerringa et al., 2012; Gerringa et al., 2020a; Yager et al., 2012). The phytoplankton community composition along the Dotson transect was dominated by haptophytes (59% to ~100%) with highest values at Stn 45 and Stn 49 (99.98 and 99.36%, respectively) (Fig. 6), whereas the Getz stations were dominated by diatoms (54–91%), especially at Stn 55 (91.3%) and Stn 24 (87.9%) (Fig. 6).

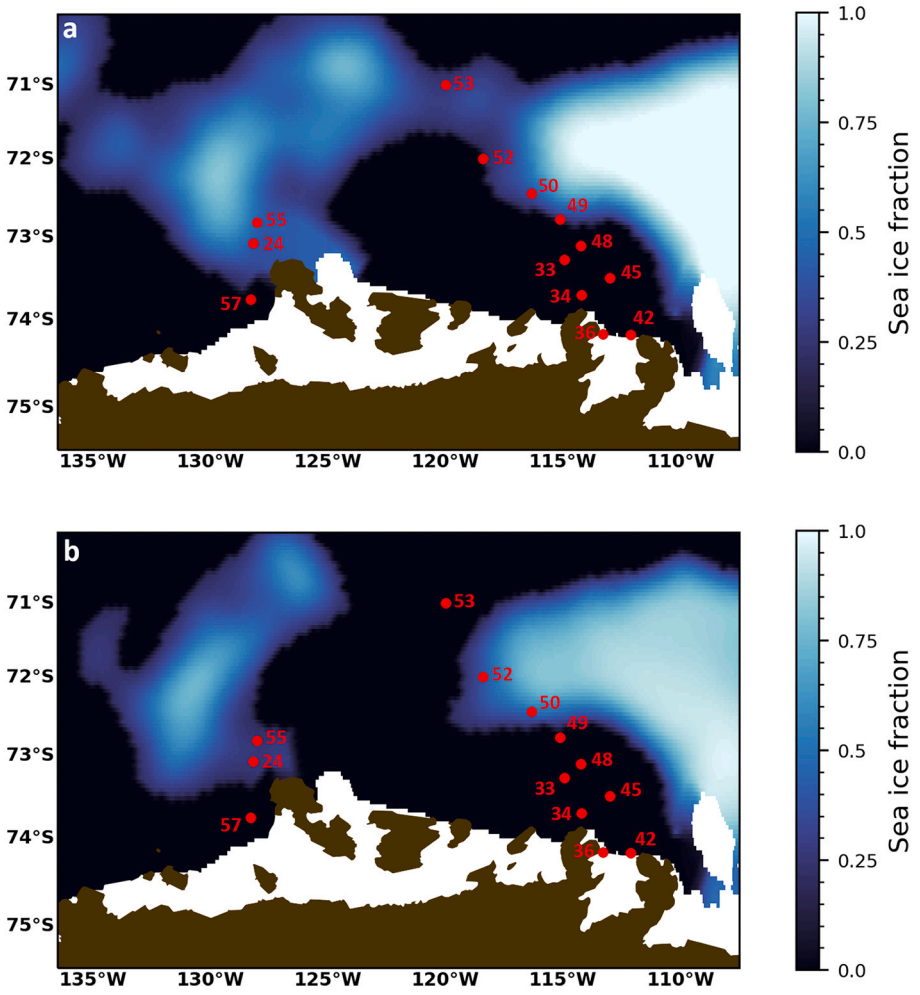

Fig. 4. Sea ice coverage during GPpr12 sampling. Data are derived from the Operational Sea Surface Temperature and Ice Analysis (OSTIA) system (0.05 × 0.05°) from **a.** the beginning of the sampling period (23-01-2018), and **b.** the end of the sampling period (02-02-2018).

3.3. Dissolved metal concentrations

Generally, dissolved Zn concentrations ([dZn]) and dissolved Cd concentrations ([dCd]) were elevated in CDW and mCDW compared to WW and AASW (Fig. 2b and c). Along the Dotson transect, [dZn] ranged from 1.22 to 8.12 nmol L^{-1} (Fig. 7a), whereas [dCd] ranged from 0.29 to 0.83 nmol L^{-1} (Fig. 8a). The highest [dZn] and [dCd] were observed close to the sea floor (~540 m) of Stn 48 (Figs. 7a and 8a), with the lowest [dZn] and [dCd] observed in the upper 50 m of most of the bloom stations (Stns 33, 34, 45, 48, 49, 50), where fluorescence was relatively high compared to the other stations (Figs. 3c, 7a, and 8a). Generally, the distribution trends of dZn and dCd were similar, with elevated [dZn] (> 5.2 nmol L^{-1}) and [dCd] (> 0.73 nmol L^{-1}) following the distribution of CDW and mCDW (Fig. 3a and b). Along the Getz transect, [dZn] and [dCd] ranged from 0.91 to 7.14 nmol L^{-1} and 0.06 to 0.79 nmol L^{-1}, respectively, with much lower dissolved concentrations of both metals observed in the upper 40 m of the off-shelf station (Stn 55) and the shelf break station (Stn 24), where fluorescence was elevated (Figs. 3f, 7d, and 8d), compared to the Dotson transect. Akin to the Dotson transect, the distribution of [dZn] followed the distribution of CDW along the Getz transect, with highest concentrations near the seafloor (Figs. 3a, b and 7d). However, in contrast to [dZn], the highest [dCd] along the Getz transect were not observed near the sea floor; instead, elevated [dCd] (0.75 to 0.79 nmol L^{-1}) were observed in the water column at 300–400 m at the off-shelf station (Stn 55), 400–500 m at the shelf break station (Stn 24), and 310–570 m at the shelf station (Stn 57) (Fig. 8d). Depth profiles of [dZn] and [dCd] at individual stations are provided in Fig. S1.

3.4. Particulate metal concentrations

3.4.1. Labile particulate metal concentrations

The distributions of LpZn and LpCd followed similar patterns; labile particulate Zn concentrations ([LpZn]) and labile particulate Cd concentrations ([LpCd]) were both generally low below 100 m along the Dotson transect and below 40 m along the Getz transect (all [LpZn] < 0.2 nmol L^{-1}; all [LpCd] < 0.01 nmol L^{-1}, Figs. 7b, e, 8b and e). In the surface layer along the Dotson transect, relatively elevated [LpZn] (> 0.7 nmol L^{-1}) and [LpCd] (> 0.08 nmol L^{-1}) were found at the off-shelf station (Stn 53) and the shelf break station (Stn 52), most mCDW inflow stations (Stns 49, 48, and 45), and most mCDW outflow stations (Stns 33 and 34) (Figs. 7b, and 8b), whereas low [LpZn] (< 0.56 nmol L^{-1}) and [LpCd] (< 0.01 nmol L^{-1}) were observed at the same depth at Stn 42 (inflow) and Stn 36 (outflow), coinciding with lower fluorescence (Fig. 3c). In the surface layer of the Getz transect, [LpZn] (> 2 nmol L^{-1}) and [LpCd] (0.2 to 0.4 nmol L^{-1}) were higher than along the Dotson transect, particularly at the off-shelf station (Stn 55) and the shelf break station (Stn 24); whereas at the shelf station (Stn 57) [LpZn] (~1.3 nmol L^{-1}) and [LpCd] (0.1 to 0.2 nmol L^{-1}) were lower than Stn 55 and Stn 24. (Figs. 7e and 8e). Depth profiles of [LpZn] and [LpCd] at individual stations are provided in Fig. S2.

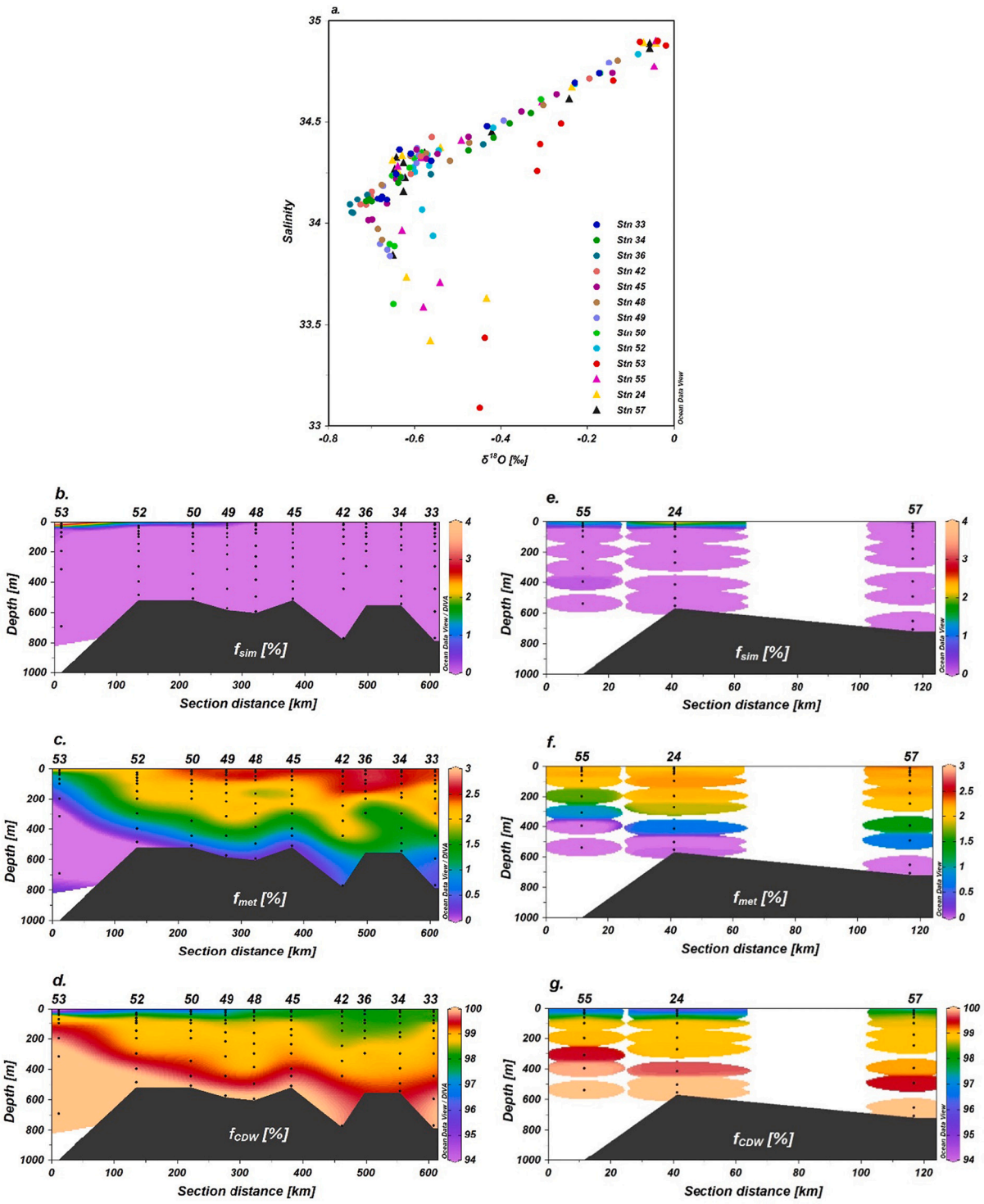

Fig. 5. GPpr12 Oxygen isotope composition ($\delta^{18}O$) versus salinity (a), and section plots of the fraction of freshwater and CDW along both transects (b–g). The fraction of sea ice melt (f_{sim}), meteoric water (f_{met}), and CDW (f_{CDW}) along the DIS transect – b. to d., and the GIS transect – e. to g. Endmembers of $\delta^{18}O$ of f_{sim}, f_{met}, and f_{CDW}, are 2.1, −25, −0.0059, respectively; whereas the endmembers of S are, 7, 0, 34.62, respectively. Note that the scales differ between Figs. 5b to 5 g.

3.4.2. *Refractory particulate metal concentrations*

Generally, refractory particulate Zn concentrations ([RpZn]) were 3 to 5 times lower than [LpZn], and refractory particulate Cd concentrations ([RpCd]) were 20 to 50 times lower than [LpCd]. Along the surface of the Dotson transect, compared to the deep, relatively elevated [RpZn] were observed at ~50 m at one of the mCDW inflow stations (Stn 45), and in the upper 20 m and at ~100 m at the mCDW outflow station (Stn 34) (Fig. 7c). Furthermore, a slight increase in [RpZn] was found at 500–550 m of Stn 42 (0.14 nmol L^{-1}) and Stn 34 (0.2 nmol L^{-1}) (Fig. 7c). Along the Getz transect, [RpZn] were generally low (<0.1 nmol L^{-1}), except for an elevation (0.17 nmol L^{-1}) at 100 m at the shelf station (Stn 57) (Fig. 7f). In the case of RpCd, elevated [RpCd] were observed in the surface layer of most stations (with the exception of Stns 42 and 36) along the Dotson transect; particularly, maxima in [RpCd] were found in the upper 50 m of the mCDW inflow station (Stn 45, 0.005 nmol L^{-1}) and the mCDW outflow station (Stn 33, 0.005 nmol L^{-1})

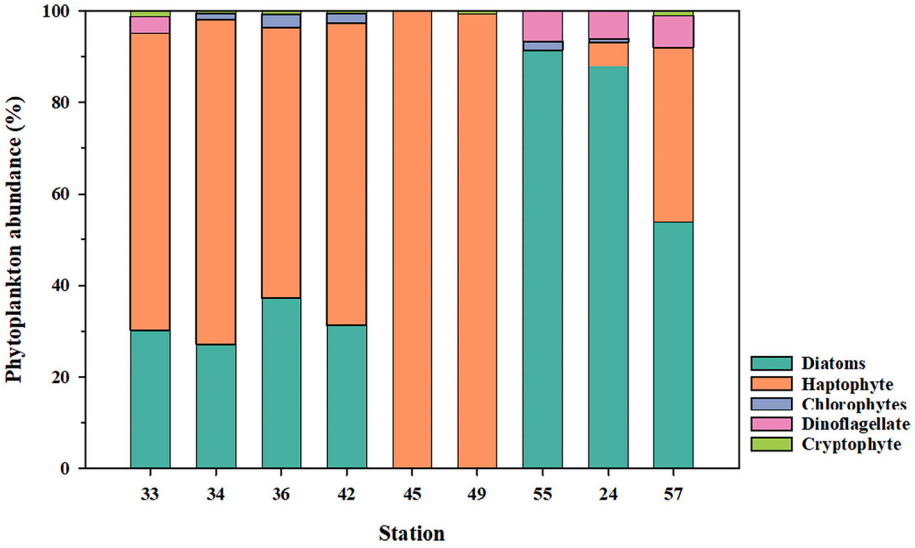

Fig. 6. Abundance of different phytoplankton groups in the surface layer along both Dotson transect (Stns 33, 34, 36, 42, 45, 49) and Getz transect (Stns 55, 24, 57).

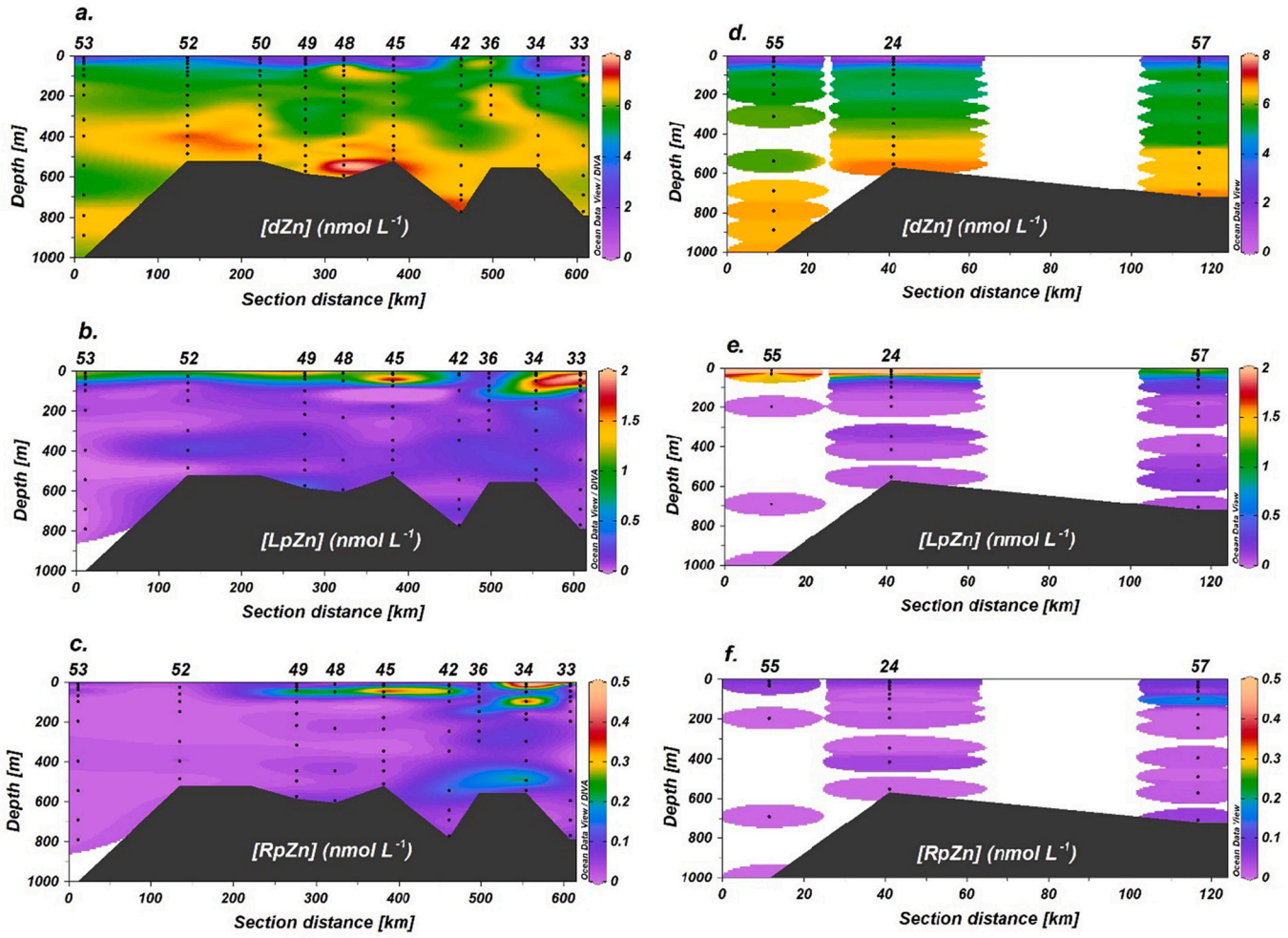

Fig. 7. GPpr12 section plots of [dZn], [LpZn], and [RpZn] (nmol L^{-1}) along both transects. Dotson transect: a. dZn, b. LpZn, c. RpZn; Getz transect: d. dZn, e. LpZn, f. RpZn. For more details on the vertical distributions, please see the vertical profiles in the Supplementary Fig. S1, S2, and S3.

(Fig. 8c). Along the Getz transect, [RpCd] were relatively elevated (~0.015 nmol L^{-1}) in the upper 40 m of the shelf break station (Stn 24) and the off-shelf station (Stn 55), whereas [RpCd] were lower (<0.007 nmol L^{-1}) at the same depth for the shelf station (Stn 57) (Fig. 8f). Below the surface later, [RpCd] were homogeneously low (< 0.001 nmol L^{-1}) along both transects. Since [RpCd] were significantly lower than

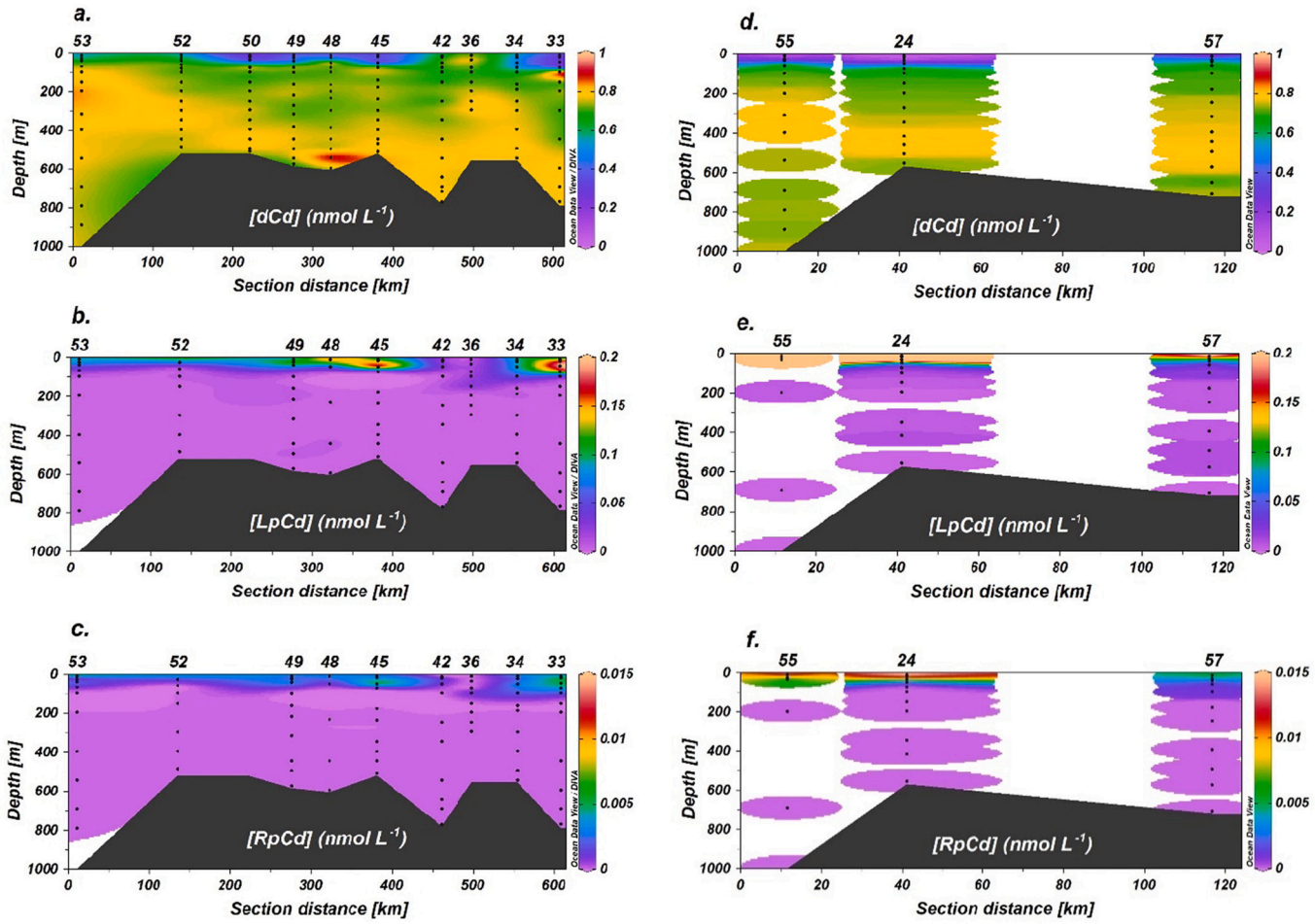

Fig. 8. GPpr12 Section plots of [dCd], [LpCd], and [RpCd] (nmol L^{-1}) along both transects. Dotson transect: a. dCd, b. LpCd, c. RpCd; Getz transect: d. dCd, e. LpCd, f. RpCd. For more details on the vertical distributions, please see the vertical profiles in the Supplementary Fig. S1, S2, and S3.

[LpCd], and RpCd has to be corrected for a LpCd contribution, such discrepancy results in a large uncertainty for measured [RpCd], especially in the surface layer where [LpCd] were elevated (see details in section 2.3.1.1). Depth profiles of [RpZn] and [RpCd] at individual stations are provided in Fig. S3.

4. Discussion

4.1. Sources of dZn, dCd, pZn, and pCd to the AS

In this study, we find that [dZn] and [dCd] are comparable to total particulate (labile + refractory) Zn and Cd concentrations ([TpZn] and [TpCd], respectively) in the surface layer, while the dissolved phase predominates over the total particulate phase at deeper depths, generally being 9 to 13 times higher (Figs. 7 and 8). This implies that scavenging by, and/or precipitation onto particles, are not dominant processes in the AS for the cycling for Zn and Cd, relative to external dissolved sources and regeneration from biogenic particles. However, external input of pZn and pCd followed by solubilization could also serve as a potential source of dZn and dCd. In order to better understand the cycling of both metals in the coastal Antarctic region, one of the objectives of this study is to assess the diverse sources of both dissolved and particulate Zn and Cd to the ASP. Here we discuss the potential sources of trace metals to our transects and the wider region, including (i) atmospheric deposition; (ii) CDW; (iii) shelf sediment sources; (iv) the Dotson Ice Shelf (meltwater induced by mCDW); (v) sea ice.

4.1.1. Atmospheric deposition

Atmospheric deposition is an important input route of trace metals to the ocean (Mahowald et al., 2018). Aerosols supply trace metals via dissolution of particles. It has also been suggested that atmospheric deposition (notably of anthropogenic particles) may be an important source for Zn and Cd in some remote oceanic regions such as the North Pacific (e.g., Liao et al., 2020) and the South Pacific (e.g., George et al., 2019). Although dust from continental landmasses and inter-hemispheric transport from the Northern Hemisphere has been observed in the surface waters of the open Southern Ocean (Li et al., 2008), it is believed that the atmospheric transport of terrigenous and anthropogenic aerosols from lower latitudes to the Antarctic region is limited because of its remoteness from non-ice covered continents (Fan et al., 2021; Gerringa et al., 2012; Gerringa et al., 2020a; Planquette et al., 2013).

In this study, [LpZn] and [LpCd] in the surface were relatively elevated compared to deeper in the water column, whereas, conversely, [dZn] and [dCd] were relatively low in the surface of both Dotson and Getz transects, except for the stations right in front of the DIS (Stns 42 and 36; Figs. 7 and 8). The low dissolved concentrations in combination with elevated LpMe implies biological uptake of both metals. On the other hand, both [RpZn] and [RpCd] in the surface were much lower than [LpZn] and [LpCd] (Figs. 7 and 8), implying little addition of lithogenic material from atmospheric deposition. In fact, [RpZn] were only relatively elevated at Stn 34 which was close to the shore (Figs. 1 and 7c), indicative of an input of lithogenic particles from the coast, rather than atmospheric deposition. For RpCd, relatively elevated

concentrations (< 0.004 nmol L^{-1}) in the surface layer at most of the bloom stations, compared to at depth (< 0.0001 nmol L^{-1}), coincided with both high fluorescence and elevated [LpCd] (Figs. 3 and 8). However, given that dust deposition is believed to be limited in this area and the lithogenic pCd only accounts for a minor fraction of the particle composition (further discussed in section 4.2), we believe that the elevation of RpCd in the surface likely result from incomplete leaching of biogenic Cd in the labile phase (perhaps relatively refractory biogenic pCd) and thus partly shows up in the refractory fraction, as the elevated RpCd was two orders of magnitude lower than LpCd (~0.2 nmol L^{-1}). Overall, we conclude that atmospheric deposition is not a significant source of either Zn or Cd to the ASP during our study, consistent with that concluded for Fe in the AS (Gerringa et al., 2012; Gerringa et al., 2020a; Planquette et al., 2013) and for Zn on the west Antarctic Peninsula (Fan et al., 2021).

4.1.2. CDW as a source of Zn and Cd to the AS region

It has been shown that CDW is a potential source of trace metals to shallower coastal Antarctic waters as it is a macro/micronutrient-rich water mass and it upwells along the continental slope or intrudes via glacial troughs (e.g., Gerringa et al., 2012; Gerringa et al., 2020a; Planquette et al., 2013; Sherrell et al., 2015). Previous work in the AS by Sherrell et al. (2015) showed [dZn] of 5 to 7 nmol L^{-1} in CDW. In this study we observed similar [dZn] within the water column where CDW was present (6.47 ± 0.39 nmol L^{-1}, mean ± 1 SD) (Fig. 2b), namely deeper than 145 m at the open ocean station (Stn 53) and deeper than 310 m at the off-shelf station (Stn 55) (Fig. 7a, and d); our observations are consistent with the previous observation that nutrient-rich CDW carried dZn into the AS (Sherrell et al., 2015).

In the case of Cd, however, although [dCd] was also elevated in CDW (0.75 ± 0.02 nmol L^{-1}, mean ± 1 SD) (Fig. 2c) at the open ocean station (Stn 53) and the off-shelf station (Stn 55), the relative dCd maximum within CDW was shallower than that of dZn (Fig. 8a and d). This could be explained by the remineralization of dZn at greater depth (Lohan et al., 2002; Zhao et al., 2014) and/or higher [dCd] in upper CDW relative to lower CDW (Sieber et al., 2019). Nevertheless, [dCd] (0.73–0.79 nmol L^{-1}, mean ± 1 SD) in CDW was generally higher than in WW and AASW (Figs. 2c), suggesting that CDW is still a source of dCd to the AS. To the best of our knowledge, there are no previous data reported on dCd in CDW in the AS region. However, [dCd] in CDW reported in this study are comparable to prior observations in the nearby Ross Sea region by Gerringa et al. (2020b), who reported an average [dCd] of 0.78 ± 0.02 nmol L^{-1} in overall mCDW and also suggested that mCDW is a source of dCd to Antarctic shelf regions.

Since our results confirm that CDW is an important source of both dZn and dCd to the AS, we estimated the flux of both trace metals from CDW to the AS. Arneborg et al. (2012) reported an estimation of the CDW flux (~0.21 Sv) in the Amundsen Sea in 2010. Based on this estimation of the CDW flux, we estimate that dZn and dCd fluxes from CDW to the AS are 4.3 × 10^7 mol $year^{-1}$ and 5.0 × 10^6 mol $year^{-1}$, respectively. However, Ha et al. (2014) reported that the CDW flux increased to ~0.34 Sv in 2011, which would correspond to the trace metal fluxes to the AS from CDW rising to 6.9 × 10^7 mol $year^{-1}$ and 8.0 × 10^6 mol $year^{-1}$ for Zn and Cd, respectively. Such large interannual variability of CDW intrusion onto Antarctic continental shelf has been attributed to not only the variability of the wind field and atmospheric circulation (Connolley, 1997; Hosking et al., 2013) but also the local Ekman pumping induced by spatial stress imbalance due to sea ice dynamics in austral summer (Kim et al., 2021). Our result shows that this interannual fluctuation of CDW intrusion may also drive large variability in the supply of dZn and dCd (and potentially other trace metals) to the AS, likely affecting the biogeochemistry and inventories of these metals in the AS.

In contrast to dZn and dCd, both LpMe and RpMe displayed consistently and extremely low concentrations within CDW at Stn 53 and Stn 55 (Figs. 7 and 8), likely since CDW is a mixture of old and deep-water masses from which most particles have settled or have been remineralized. Therefore, CDW does not appear to be a source of pZn or pCd to the AS.

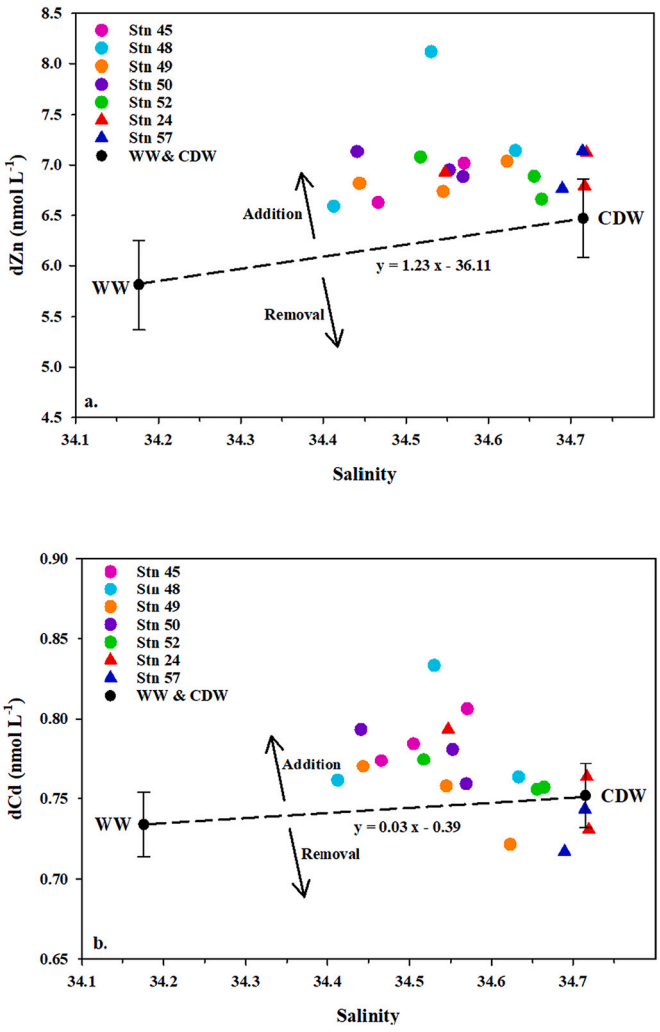

Fig. 9. [dZn] and [dCd] versus salinity (S) close to the AS seafloor (~ 100 m). a. [dZn] versus S. b. [dCd] versus S. The black circles represent the average dissolved metal, as well as average salinity for both WW and CDW. Average values were selected based on Θ-S diagram (Fig. 2) and section profiles (Figs. 7a, d, 8a, and d). The endmembers (mean ± 1SD) for S, [dZn], and [dCd], in WW and CDW are – S_{WW}: 34.18 ± 0.03, $[dZn]_{WW}$: 5.81 ± 0.44 nmol L^{-1}, $[dCd]_{WW}$: 0.73 ± 0.02 nmol L^{-1}; S_{CDW}: 34.72 ± 0.03, $[dZn]_{CDW}$: 6.47 ± 0.39 nmol L^{-1}, $[dCd]_{CDW}$: 0.75 ± 0.02 nmol L^{-1}. The dashed lines represent the mixing line between WW and CDW.

4.1.3. Sedimentary input of Zn and Cd to mCDW at depth

Based on the observation of high [dZn] and [dCd] in mCDW (Figs. 3, 7, and 8), we are confident that the intrusion of nutrient rich CDW brings trace metal-rich waters onto the continental shelf that are subsequently mixed with overlying, relatively trace metal-poor seawater, with relatively high [dZn] and [dCd] present even after mixing (Figs. 7 and 8). Since mCDW travels along the seafloor of the continental shelf (Fig. 3), sedimentary input induced by particle (and porewater) resuspension or porewater diffusion might supply additional dZn and dCd to mCDW (Schmitt et al., 2009; Sherrell et al., 2015). However, such sedimentary input was suggested to be only a modest source for dZn in the AS, relative to incoming CDW (Sherrell et al., 2015). To assess whether sediment-derived dZn and dCd is added to mCDW along its transport path, as well as to quantify any such contributions, we evaluated the conservative mixing lines in waters up to 100 m above the seafloor at

Table 3
Endmembers and the output of the three-endmember mass balance approach used in section 4.1.4. The symbols f', δ', S, and M denote the fraction (%), weight-averaged $\delta^{18}O$ (‰), salinity, and weight-averaged metal concentration (nmol L^{-1}) (mean ± 1 SD), respectively, whereas *IS*, *inflow*, *sw* and *outflow*, stand for the observed values in ice shelf meltwater, mCDW inflow, shelf water, mCDW outflow, respectively. a: $\delta^{18}O$ value in ice shelf is used from Randall-Goodwin et al., 2015. b: values are calculated based on the interpolation of $\delta^{18}O$ between 442 m and 507 m as $\delta^{18}O$ at 467 m was not analyzed.

Endmembers										
Ice shelf (IS)		δ	S	f'_{IS}	f'_{inflow}	f'_{sw}				
		-25[a]	0	0.6	74.9	24.5				
	station	depth (m)	δ'	S	M_{dZn}	M_{dCd}	M_{LpZn}	M_{RpZn}	M_{LpCd}	M_{RpCd}
	45	442	−0.27	34.47	6.63	0.77	0.10	0.028	0.003	0.0001
	45[b]	467	−0.22	34.51	6.98	0.78	0.11	0.033	0.003	0.0001
	45	507	−0.14	34.57	7.02	0.81	0.14	0.042	0.003	0.0001
mCDW inflow	bottom	520								
	48	592	−0.13	34.63	7.14	0.76	0.15	0.068	0.003	0.0001
	bottom	605								
	wt. avg		−0.18 ± 0.07	34.57 ± 0.091	7.01 ± 0.19	0.77 ± 0.01	0.13 ± 0.03	0.05 ± 0.03	0.003 ± 0.001	0.0001 ± 0.0001
	45	176	−0.55	34.18	5.75	0.74	0.13	0.029	0.004	0.0001
shelf water (sw)	45	235	−0.60	34.20	5.97	0.74	0.04	0.031	0.004	0.0001
	bottom	238								
	wt. avg		−0.55 ± 0.03	34.18 ± 0.014	5.76 ± 0.16	0.74 ± 0.01	0.12 ± 0.06	0.029 ± 0.001	0.004 ± 0.001	0.0001 ± 0.0001
mCDW outflow	36	294	−0.44	34.22	6.69	0.79	0.10	0.092	0.004	0.0001

Output (all units are in nmol L^{-1}, mean ± 1 SD)					
dZn_{IS}	$dZn_{IS} \times f'_{IS}$	$LpZn_{IS}$	$LpZn_{IS} \times f'_{IS}$	$RpZn_{IS}$	$RpZn_{IS} \times f'_{IS}$
5.3 ± 0.6	0.034 ± 0.004	−4.95 ± 3.62	−0.03 ± 0.02	7.33 ± 4.27	0.047 ± 0.027
dCd_{IS}	$dCd_{IS} \times f'_{IS}$	$LpCd_{IS}$	$LpCd_{IS} \times f'_{IS}$	$RpCd_{IS}$	$RpCd_{IS} \times f'_{IS}$
4.5 ± 0.3	0.029 ± 0.002	0.09 ± 0.01	0.001 ± 0.001	0.015 ± 0.004	0.0001 ± 0.0001

stations located on the continental shelf and the shelf break (Fig. 9).

Based on the Θ-S diagram and section profile of the inflow (Fig. 2a and 3), WW and CDW were the two primary water masses involved in mixing over this depth range (100 m above the seafloor). Assuming that WW and CDW were the only two components of mCDW, changes in [dZn] and [dCd] in mCDW should follow the mixing line of WW-CDW if distributions of the metals were only controlled by conservative mixing. The endmembers for salinity (S), [dZn], and [dCd] used for this mixing line are the average values (mean ± 1 SD) of WW (S_{WW}: 34.18 ± 0.03, $[dZn]_{WW}$: 5.81 ± 0.44 nmol L^{-1}, $[dCd]_{WW}$: 0.73 ± 0.02 nmol L^{-1}) and CDW (S_{CDW}: 34.72 ± 0.03, $[dZn]_{CDW}$: 6.47 ± 0.39 nmol L^{-1}, $[dCd]_{CDW}$: 0.75 ± 0.02 nmol L^{-1}) respectively. Specifically, the endmember for CDW is selected from the observed salinity from this study (Stns 53 and 55, where the least modified CDW was located), rather than using the value reported by Randall-Goodwin et al. (2015) as used for freshwater calculation in section 3.1.2. This is because there is no reported [dZn] endmember data for pure CDW in this region and this calculation assesses the effects of mixing between local, already partly modified water masses. This mixing line can then be used differentiate and quantify any local input (source; points above the mixing line) or output (sink; points below the mixing line) (Fig. 9).

In the case of dZn, all samples from both the Dotson and Getz transect plot above the mixing line (Fig. 9a), indicating a consistent external dZn source to mCDW along both transects. By calculating the average difference between the mixing line and individual samples, we estimate that this Zn source supplies ~0.42 ± 0.22 nmol L^{-1} (mean ± 1 SD) of dZn to mCDW. This result agrees with previous suggestions that benthic input supplies modest dZn to the AS (Sherrell et al., 2015), compared to dZn originating within CDW. This additional Zn source could result from sediment resuspension followed by desorption and/or porewater diffusion (e.g., Conway and John, 2014; Lemaitre et al., 2020). The same assessment for dCd, however, suggests only limited sedimentary dCd input at most stations along the Dotson transect (0.030 ± 0.023 nmol L^{-1}, mean ± 1 SD) (Fig. 9b). However, because of the order of magnitude difference in [dZn] and [dCd] in mCDW, such sedimentary addition corresponds to a relatively similar 7% and 4% addition of [dZn] and [dCd], respectively. In contrast, along the Getz transect, the near-bottom samples at Stn 24 and Stn 57 plot below the mixing line with an estimated dCd reduction of 0.025 ± 0.016 nmol L^{-1} (mean ± 1 SD), showing effectively no source of dCd to the Getz transect. Thus, when compared to dZn, our results show that the sedimentary input of dCd is spatially variable in the AS. Along the Dotson transect, we estimated the sedimentary fluxes for both Zn and Cd required to match the observed data, assuming the volume of CDW intrusion onto the continental shelf remains constant; estimated sedimentary trace metal fluxes are about 4.5×10^6 mol $year^{-1}$ and 3.2×10^5 mol $year^{-1}$ of dZn and dCd to the overlying water, based on the calculated CDW flux in the AS in 2011 (Ha et al., 2014). However, it should be noted that these values are first-hand estimates which are likely to vary since the spatial and temporal variability of sedimentary fluxes are unknown in the region.

In the case of the particulate metals, both [LpZn] and [LpCd] decreased with depth ([LpZn] < 0.2 nmol L^{-1}; [LpCd] < 0.01 nmol L^{-1}, Figs. 7b, e, 8b and e) compared to the surface layer along both transects and near-bottom. Similarly, [RpCd] were extremely low at depth (< 0.01 nmol L^{-1}) along both transects (Fig. 8c and f), implying that sedimentary input does not contribute a significant amount of LpZn, LpCd, or RpCd to the water column and/or regeneration of labile particles at depth. On the other hand, [RpZn] is elevated between 400 and 600 m at the near-shore area (0.15–0.20 nmol L^{-1}, Stns 42 and 34) (Fig. 7c), suggesting a source of RpZn limited to shelf sediments near the ice shelf which potentially consists of glacial particles (terrestrial input).

4.1.4. The influence of the DIS on dissolved metals in the AS

Ice shelves are considered sources of both dissolved and particulate trace metals, with potential offshore transport of these metals. For example, it has been suggested that basal melt beneath the DIS adds dissolved Fe (Alderkamp et al., 2015; Sherrell et al., 2015; Yager et al., 2012) as well as particulate Fe (van Manen et al., 2022) to underlying waters. Additionally, the outflowing mCDW from underneath ice shelves may carry sediment-derived and ice shelf-derived particles into Antarctic coastal waters – Herraiz-Borreguero et al. (2016) found significant Fe input from the Amery Ice Shelf due to the melting of marine ice (i.e.

an accreted ice layer formed by supercooling of accumulated frazil ice platelets underneath the ice shelf) potentially containing fine sediments and biogenic materials. However, whether the melting of ice shelves could be a source of dissolved and particulate Zn and Cd to Antarctic coastal waters remains practically unknown. Previously, Sherrell et al. (2015) suggested that mCDW outflow from the DIS brings only modest amounts of dZn to the Amundsen Sea. For dCd, there is no evidence showing that the DIS melting adds Cd to mCDW outflow, however, Sieber et al. (2019) suggested a Cd input associated with the meltwater of the Mertz Glacier to nearby surface waters in East Antarctica.

In our study, according to the distribution of salinity, temperature, and $\delta^{18}O$ (Figs. 3 and 5) the inflowing mCDW (with additional sediment derived trace metals, see section 4.1.3) was characterized close to the floor of the continental shelf (~500 m), whereas the outflowing mCDW was observed between 200 and 400 m, which is in general agreement with previous observations (Miles et al., 2016; Randall-Goodwin et al., 2015), although the depth can change depending on the geographical location. In addition to the mCDW inflow, mCDW outflow, and ice shelf meltwater, the water at the edge of the DIS (a mixture of WW and AASW, hereby referred to as shelf water) also plays an important role in the cycling of metals in the ice shelf system due to physical mixing process (van Manen et al., 2022). Here, we utilized a similar three-endmember mass balance approach to that described in section 3.1.2, but with different (local) endmembers. Assuming physical mixing between three water masses – mCDW inflow, shelf water, and ice shelf meltwater to be the main mechanism that alters dissolved metal concentrations, the equations from Section 3.1.2 were modified:

$$f'_{IS} + f'_{inflow} + f'_{sw} = 1 \quad (4)$$

$$f'_{IS} \times \delta_{IS} + f'_{inflow} \times \delta_{inflow} + f'_{sw} \times \delta_{sw} = \delta_{outflow} \quad (5)$$

$$f'_{IS} \times S_{IS} + f'_{inflow} \times S_{inflow} + f'_{sw} \times S_{sw} = S_{outflow} \quad (6)$$

$$f'_{IS} \times M_{IS} + f'_{inflow} \times M_{inflow} + f'_{sw} \times M_{sw} = M_{outflow} \quad (7)$$

Here, f', δ, S, and M denote the volume fraction, endmember $\delta^{18}O$ value, salinity, and endmember metal concentration, respectively, using depth-weighted averages (i.e. data integrated over depth and divided by the depth of (part of) the water column to account for unequal spacing between sampled depths). The terms *IS*, *inflow*, *sw* and *outflow*, stand for ice shelf meltwater, mCDW inflow, shelf water, and mCDW outflow, respectively. To get four unknowns (f'_{IS}, f'_{inflow}, f'_{sw}, and M_{IS}), the other endmembers were defined based on observations or previously reported values (Table 3). For the mCDW inflow, the endmembers were defined based on Stn 45 and Stn 48 (between the sediments and 100 m above the seafloor). Please note that the endmembers of δ and S of mCDW used here are different than the CDW endmembers used in section 3.1.2 that is based on values reported by Randall-Goodwin et al. (2015) for consistency with previous studies. The purpose of the earlier calculation was to evaluate the freshwater input (sea ice melt water and ice shelf melt water). However, in this section (4.1.4), the aim is instead to assess the mixing of inflowing mCDW, ice shelf melt water, outflowing mCDW, and shelf water at a much smaller scale and thus we choose the endmembers based on observations in this study. For shelf water, the endmembers were chosen based on temperature ($\Theta < -1.5$ °C) at Stn 45 (72–235 m) (Table 3). Depths from 72 m to 136 m at Stn 45 were excluded in this definition due to high production of labile particles produced from intense biological activity. Stn 42 was also excluded in the selection for both mCDW inflow and shelf water as it is strongly influenced by terrestrial input, based on observation of elevated [dFe] during the sampling interval (van Manen et al., 2022). For the mCDW outflow, the endmembers were chosen from the first outflow station (Stn 36, 294 m) (Fig. 3 and Table 3). Using this approach, the output ($f'_{IS} \times M_{IS}$) gives a first order estimate of the concentration contributed by ice shelf melt – a positive value would imply ice shelf melt contributes dissolved metals to mCDW outflow, whereas a negative value would imply net removal. Using this approach, however, it is important to note a potential caveat – that the mCDW endmember (i.e., concentrations) may be something of an underestimation as mCDW may acquire more sediment derived metals between Stn 45 and the ice shelf, resulting in an effective overestimation of the contribution of ice shelf derived metal concentrations to the outflow.

The results of our calculation show that the mCDW outflow is composed of 0.6% ice shelf meltwater (f'_{IS}), 24.5% shelf water (f'_{sw}), and 74.9% of mCDW inflow (f'_{inflow}), with positive ($f'_{IS} \times M_{IS}$) values (Table 3), implying a contribution of both metals from ice shelf melt. In the case of Zn, estimated [dZn] (M_{IS}) in the ice shelf meltwater (5.3 ± 0.6 nmol L^{-1}, mean ± 1 SD) are lower than other water masses involved in the mixing (Table 3), with an estimated input ($f'_{IS} \times M_{IS}$) of 0.034 nmol L^{-1} (Table 3). This implies that the ice shelf meltwater is not a relatively important source of dZn, even though there is a large uncertainty on this estimate and the endmember. Furthermore, [dZn] in shelf water (5.76 ± 0.16 nmol L^{-1}) was lower than in the incoming mCDW (7.01 ± 0.19 nmol L^{-1}); whereas the mCDW outflow (6.69 nmol L^{-1}) appeared to be comparable to – or even slightly lower than – the mCDW inflow (although given the single observation available to estimate the outflow endmember, this cannot be stated with certainty); this observation also implies that DIS meltwater does not add a significant amount of dZn, instead suggesting an effective dilution by mixing with shelf water once the outflowing mCDW leaves from underneath the DIS, similar to recent observations for Fe (van Manen et al., 2022). On the other hand, estimated [dCd] (M_{IS}) in the ice shelf meltwater (4.5 ± 0.3 nmol L^{-1}) are much higher than in other water masses (Table 3), implying that the DIS could be a relatively strong source of dCd to the outflowing mCDW. However, the overall [dCd] in the inflow and outflow are similar (Table 3), and it is estimated that DIS melt only adds 0.029 ± 0.001 nmol L^{-1} of dCd to the outflow concentration of 0.79 nmol L^{-1}, likely due to a small contribution of meltwater (0.6%). The same calculations were also done for both fractions of particulate metals. A negligible contribution (or minor removal) is estimated from ice shelf melt ($f'_{IS} \times M_{IS}$, [LpZn]: −0.03 ± 0.02 nmol L^{-1}, [RpZn]: 0.047 ± 0.027 nmol L^{-1}, [LpCd]: 0.001 ± 0.001 nmol L^{-1}, and [RpCd]: 0.0001 ± 0.0001 nmol L^{-1}) (Table 3). In a previous study, Sieber et al. (2019) suggested that glacial melt water may contribute dCd to surface waters from the Mertz Glacier (east Antarctica), possibly originally in particulate form. However, input of pCd from the DIS in the ASP is not observed in the current study.

Our results thus suggest that DIS melt is only a negligible source of dZn and dCd, which agrees with the findings of Sherrell et al. (2015), and that DIS melt is not a discernible source of pZn and pCd. However, the caveat of this approach is that it is based solely on physical mixing with best estimates for the endmembers involved. From the measurements in this study, we are unable to quantify any biogeochemical process (e.g., adsorption onto particles and regeneration) or physical processes (e.g., particle settling) that might remove/add both metals underneath DIS. To further investigate this issue, a more direct proxy than dissolved metal concentrations is required, such as trace metal isotope ratios that could help to differentiate between coinciding metal sources and sinks during mCDW-induced ice sheet melt (e.g., Sieber et al., 2019; Sieber et al., 2020).

4.1.5. Sea ice as a negligible source of dissolved metals to the ASP

Sea ice is considered an important local source of trace metals in the polar regions, notably for Fe (Arrigo et al., 1997; Duprat et al., 2020; Lannuzel et al., 2008; Lannuzel et al., 2010; Moreau et al., 2019; Sedwick and DiTullio, 1997). Although observations for Zn and Cd in sea ice are relatively scarce, Lannuzel et al. (2011) reported that dZn and dCd are not particularly enriched in sea ice near East Antarctica, relative to seawater concentrations, suggesting that sea ice is not a significant source of dZn and dCd to surface waters in that region. However, given the strong melt of sea ice in the AS during the period of sampling (Fig. 4),

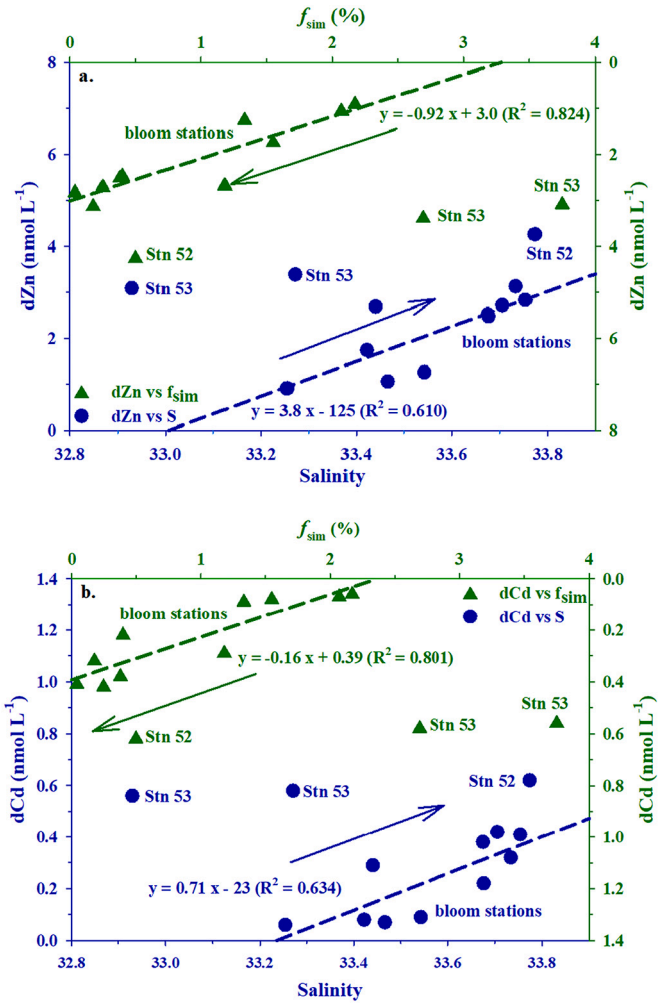

Fig. 10. [dZn] and [dCd] versus salinity (in blue) and the fraction of sea ice melt (f_{sim}) (in green) at the surface (~ 20 m) of the open ocean station (Stn 53), the shelf break station (Stn 52) and the bloom stations (Stn 50, 49, 48, 55, 24, 57). a. [dZn] b. [dCd]. The regression lines show significant trends (all p values <0.05) excluding Stn 52 and 53 and the arrows indicate the direction of the trends.

sea ice melt might be a source of trace metals, especially in the offshore area. In this study, several stations (Stns 53, 52, 50, 49, 55, and 24) were located within the sea ice or on the edge of the sea ice region (Fig. 4). Furthermore, a positive sea ice melt fraction was found in the upper 20 m of these stations, as well as at Stn 48 and Stn 57 (Fig. 5), suggesting these stations are subject to the influence of sea ice melt. To further evaluate the influence of sea ice melt on the metal concentrations in the surface (~20 m), the open ocean station (Stn 53), the shelf break station (Stn 52), and the bloom stations (Stns 50, 49, 48, 55, 24, and 57) are selected for comparison.

If sea ice melt were a strong source and the main driver of dissolved metal concentrations in the surface, both [dZn] and [dCd] should co-vary with salinity and f_{sim} (i.e. concentrations increase with decreasing salinity and increasing f_{sim}). However, [dZn] and [dCd] in the region with a positive f_{sim} display an increasing trend with increasing salinity and decreasing f_{sim} (Fig. 10). Additionally, in the surface layer, higher metal concentrations are observed at the non-bloom stations, whereas at the bloom stations lower metal concentrations are found (Figs. 3, 7, and 8). This implies that the dissolved metal concentrations in the upper 20 m in the region with a positive f_{sim} are not only influenced by sea ice melt, but predominantly controlled by other processes – biological uptake and/or sorption onto (biogenic) particles, which is supported by increasing LpMe observed at the bloom stations (Figs. 3, 7, and 8). This complicates any assessment of sea ice melt as a metal source, since biological uptake and scavenging processes could balance out any primary contribution from sea ice melt. Nevertheless, with the parameters obtained in this study, we speculate that sea ice melt is not a strong source of either dZn or dCd in the AS. Similar observations are reported for sea ice in East Antarctic waters (Lannuzel et al., 2011). This is in contrast to observations in Arctic sea ice which is found to be enriched in Zn and Cd, compared to surface seawater and therefore suggested to be a significant source to seawater (Tovar-Sánchez et al., 2010). The discrepancy between Arctic and Antarctic sea ice might result from the influence of anthropogenic (and dust) aerosol deposition in the Arctic – for example, Marsay et al. (2018) found Zn and Cd in aerosol particles collected in the Arctic region to be significantly higher than crustal values, implying the transport of anthropogenic aerosols from nearby landmasses. More direct measurements, such as metal concentrations in sea ice and meltwater, and other proxies such as metal stable isotopic composition, are needed to further unravel the dynamics of dissolved metals and assess the relative influence of chemical (e.g., biological assimilation and sorption) and physical (e.g., mixing with underlying waters) processes in Antarctic coastal regions.

Likewise, since biological activity is dominant in the surface layer, leading to a significant production of labile particles, it is impossible to distinguish whether sea ice melt released LpZn and LpCd to the surface or not, based on the available data. In contrast to labile particles, refractory particles are not expected to be produced or influenced by biological activity, and RpZn and RpCd at the stations located within the sea ice or on the edge of the sea ice region (Stn 53, 52, 50, 49, 55, and 24) are consistently low ([RpZn]: ~0.1 nmol L^{-1}, [RpCd]: < 4 pmol L^{-1}) in the upper 20 m. Based on these low refractory concentrations, we thus conclude that sea ice melt is not a strong source of RpZn and RpCd. Nevertheless, [RpCd] in the surface layer were elevated compared to deeper water, suggesting there might be a small source of RpCd. However, as noted with our assessment of this for atmospheric deposition, the much higher labile concentrations lead to a large uncertainty in the determination of the refractory fraction (see section 2.3.1.2); this effect, in addition to the possibility of incomplete leaching of LpCd as noted in section 4.2.2.2, means a minor contribution from sea ice melt cannot be ruled out based on the current data.

To sum up, CDW, together with sedimentary input (7% for dZn and 4% for dCd in the DIS region), is the main source for both dZn and dCd to the AS, whereas neither atmospheric deposition nor sea ice melt seem to supply either dissolved metal to the water column, and the effect of ice shelf melt is convoluted by water mass mixing process. Our results imply that the increasing flux of warm CDW intruding into the AS (Jacobs et al., 2011) could potentially increase the flux of both dZn and dCd, by enhancing the ice shelf melt-driven circulation (meltwater pump, St-Laurent et al., 2017), affecting the biogeochemical cycling of the ASP. Such stronger circulation would increase the supply via both mCDW upwelling (with its sedimentary derived component) and any supply from the ice shelf. Although particulate metals are only a relatively minor component of the overall metal pool in this study, especially below the surface layer, biogenic particles could play an important role in the cycling of dZn and dCd in the upper ocean due to varying uptake by different phytoplankton communities, as discussed in the next sections.

4.2. *Particle composition*

The highest [LpZn] and [LpCd] were found in surface waters, notably at the bloom stations, coinciding with relatively low [dZn] and [dCd]. In these locations, [LpZn] and [LpCd] were sometimes roughly equal to [dZn] and [dCd] (Figs. 7 and 8); this observation likely indicates strong biological uptake of dissolved metals and/or scavenging onto suspended particles. Additionally, the phytoplankton biomass (indicated by fluorescence and elevated particulate P concentrations; Fig. 3 and

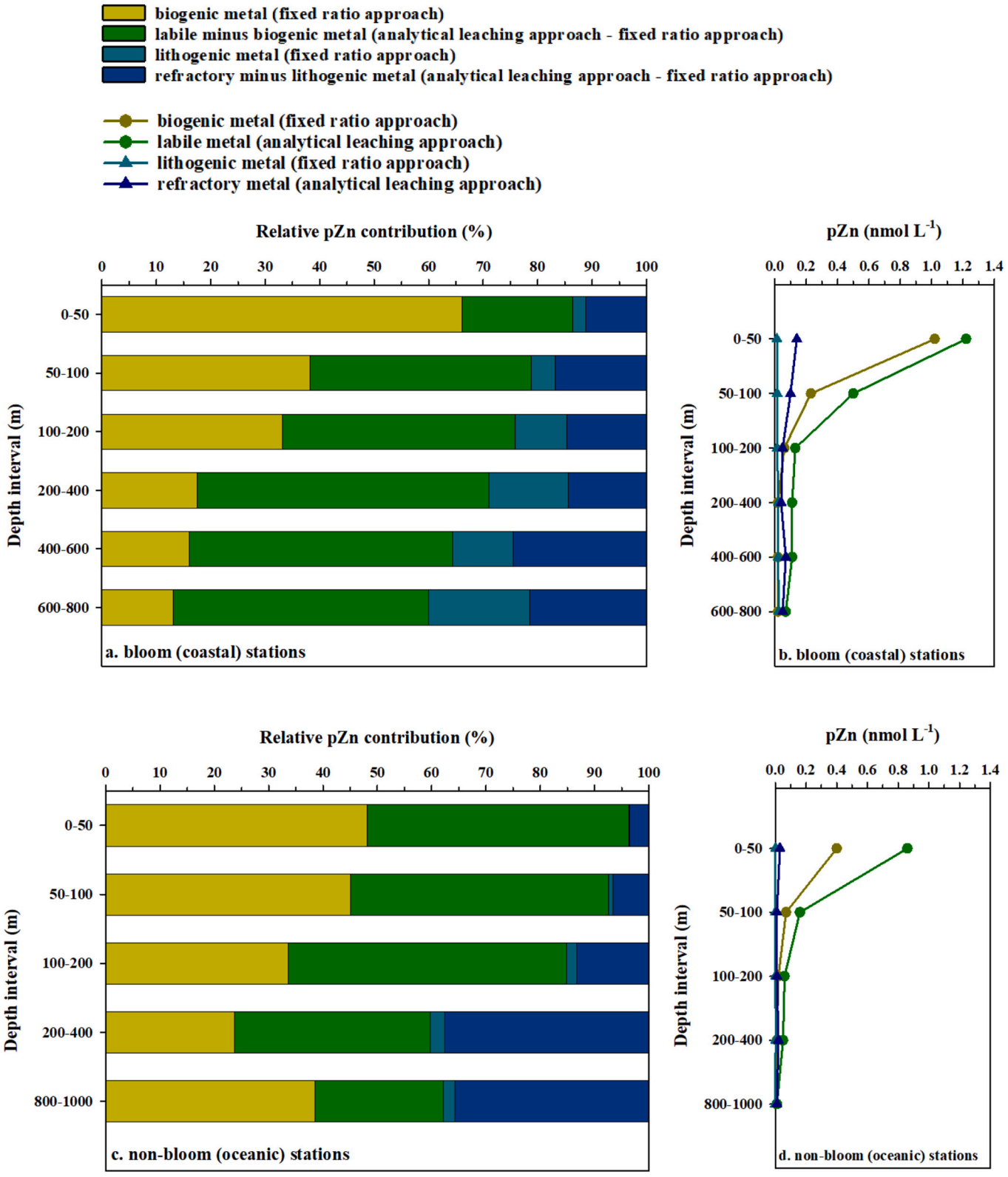

Fig. 11. Relative contributions and concentrations of biogenic, labile, lithogenic, and refractory fractions at both bloom (coastal) stations and non-bloom (oceanic) stations during GPpr12. Biogenic and lithogenic contributions (and concentrations) were calculated using the 'fixed ratio approach', whereas labile and refractory contributions (and concentrations) were calculated using the analytical leaching approach. a. and c. relative biogenic pZn contributions. b. and d. biogenic pZn concentrations. e. and g. relative biogenic pCd contributions. f. and h. biogenic pCd concentrations. Each contribution is calculated based on the corresponding ratios described in section 4.2.2.

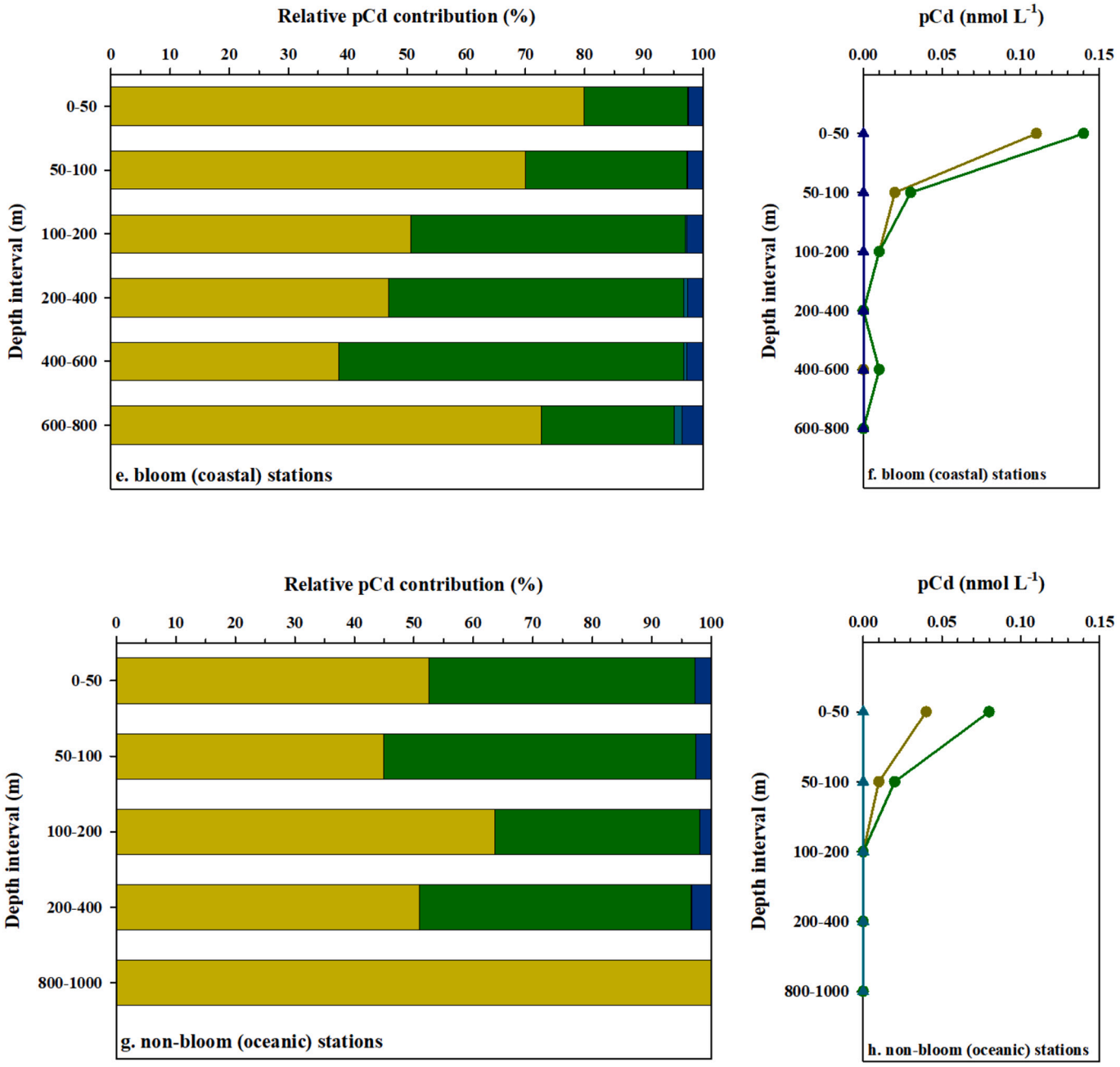

Fig. 11. (*continued*).

Supplements Fig. S2) was also relatively high at these stations. Generally, there are multiple pathways for bio-active metals to partition between the dissolved phase and the particulate phase – biological assimilation, adsorption onto particles (e.g., biogenic/authigenic/abiotic particles), competition between metal binding ligands and particles, and remineralization (e.g., Bruland et al., 2013). The importance of each process varies per metal depending on the environmental conditions (e.g., biological activity and redox conditions), which could alter the compositions of particulate metals. Furthermore, particulate metal compositions can also be controlled by external sources and interactions near the sea floor, such as sediment resuspension and authigenic mineral formation (e.g., Planquette et al., 2013; Raiswell et al., 2016). To understand the interaction between dissolved and particulate phases, we discuss (i) the origins of particles collected in the surface layer, and (ii) quantify both the concentrations of biogenic and lithogenic particles as well as the relative contributions to the total particulate metal pool.

4.2.1. *Particle origins based on relationships with Al and P*

To assess the origin of particles, we assumed all P in the particles was biogenic and all Al was from lithogenic materials (e.g., Planquette et al., 2013). The total particulate Zn (TpZn), total particulate Cd (TpCd), total particulate P (TpP), total particulate Al (TpAl), and the interrelationships between these quantities can then be used to assess whether there is a consistent biogenic or lithogenic fraction of Zn and Cd. With the intercept not forced through 0, the regression between TpMe and TpP indicates that biogenic metals dominate the TpMe pools in the surface layer at both the bloom stations ($R^2_{TpZn\text{-}TpP} = 0.69$, $R^2_{TpCd\text{-}TpP} = 0.88$, $n = 37$, both $p < 0.05$) and the non-bloom stations ($R^2_{TpZn\text{-}TpP} = 0.66$, $R^2_{TpCd\text{-}TpP} = 0.85$, $n = 8$, both $p < 0.05$). Subsequently, the coefficient of determination (R^2) decreases below the surface layer (Supplementary Table S1), suggesting a smaller contribution of particles of biogenic origin to the overall particulate pool, likely due to remineralization of biogenic particles. Interestingly, at the bloom stations, the R^2

Table 4
Estimated biogenic and lithogenic metal concentrations in the AS estimated by two approaches. Concentrations (mean ± 1 SD) are calculated from samples within corresponding depth intervals. All units are in nmol L^{-1} except the ones labeled with "a" (in pmol L^{-1}). See Section 4.2.2 for more details.

		fixed ratio approach				analytical leaching approach			
		biogenic [pZn]	lithogenic [pZn][a]	biogenic [pCd]	lithogenic [pCd][a]	labile [pZn] (biogenic)	refractory [pZn][a] (lithogenic)	labile [pCd] (biogenic)	refractory [pCd][a] (lithogenic)
GPpr12 Bloom (coastal) stations	0–50 m (n = 10)	1.02 ± 0.76	13 ± 12	0.11 ± 0.08	0.02 ± 0.02	1.22 ± 0.61	139 ± 77	0.14 ± 0.10	3.91 ± 3.00
	50–100 m (n = 8)	0.23 ± 0.22	15 ± 13	0.02 ± 0.02	0.02 ± 0.02	0.50 ± 0.51	105 ± 106	0.03 ± 0.04	1.02 ± 1.13
	100–200 m (n = 8)	0.06 ± 0.06	14 ± 11	0.01 ± 0.01	0.02 ± 0.01	0.13 ± 0.08	46 ± 45	0.01 ± 0.01	0.27 ± 0.20
	200–400 m (n = 7)	0.02 ± 0.01	22 ± 17	< 0.01	0.03 ± 0.02	0.11 ± 0.05	44 ± 28	0.01 ± 0.01	0.16 ± 0.04
	400–600 m (n = 8)	0.02 ± 0.01	21 ± 17	< 0.01	0.03 ± 0.02	0.11 ± 0.06	69 ± 62	0.01 ± 0.01	0.20 ± 0.08
	600–800 m (n = 3)	0.02 ± 0.01	23 ± 7	< 0.01	0.03 ± 0.01	0.07 ± 0.01	50 ± 13	< 0.01	0.12 ± 0.01
	Average	0.23 ± 0.40	18 ± 5	0.02 ± 0.04	0.02 ± 0.01	0.36 ± 0.45	75 ± 38	0.03 ± 0.05	0.95 ± 1.49
GPpr12 non-bloom (oceanic) stations	0–50 m (n = 2)	0.40 ± 0.13	0.89 ± 0.27	0.04 ± 0.01	< 0.01	0.86 ± 0.21	33 ± 15	0.08 ± 0.01	2.19 ± 0.09
	50–100 m (n = 2)	0.07 ± 0.03	1.08 ± 0.22	0.01 ± 0.01	< 0.01	0.16 ± 0.08	13 ± 7	0.02 ± 0.01	0.51 ± 0.36
	100–200 m (n = 2)	0.02 ± 0.01	1.38 ± 0.94	< 0.01	< 0.01	0.06 ± 0.01	11 ± 1	< 0.01	0.09 ± 0.04
	200–400 m (n = 2)	0.01 ± 0.01	2.18 ± 2.58	< 0.01	< 0.01	0.05 ± 0.05	19 ± 5	< 0.01	0.09 ± 0.06
	800–1000 m (n = 1)	0.01	0.34	< 0.01	< 0.01	0.01	6	< 0.01	0.05
	Average	0.10 ± 0.17	1.2 ± 0.7	< 0.01	< 0.01	0.23 ± 0.36	17 ± 10	0.02 ± 0.03	0.59 ± 0.91

value for Cd remains high below the surface layer, while that for Zn decreases more notably (Supplementary Table S1). This difference suggests there may be a phase of abiotic pZn (e.g. sedimentary or scavenging-derived pZn) that increases with depth, whereas it is not a dominant process for pP and pCd (details discussed in section 4.2.2). On the other hand, the coefficients of determination of the regressions between TpMe and TpAl in the surface layer of the bloom stations are comparable ($R^2_{TpZn\text{-}TpAl} = 0.36$, $R^2_{TpCd\text{-}TAl} = 0.41$, n = 37, both $p < 0.05$), and slightly increases for TpZn-TpAl (but not TpCd-TpAl) below the surface layer, (Supplementary Table S1). Together with the weakening regression between TpZn and TpP below the surface layer, this result implies lithogenic pZn becomes more prevalent at depth in the AS, whereas this effect is less profound for pCd.

4.2.2. Estimated biogenic (and lithogenic) metal concentrations and relative contributions

The varying regression between TpMe and TpP (and TpMe-TpAl) only indicates relative changes in particle composition and inferred origin – quantifying the concentrations of particles of biogenic and lithogenic origin requires further investigation. To date, there are several common approaches taken to estimate biogenic and lithogenic components of bulk particles. The first approach is to separate bulk particles into labile and refractory fractions by using chemical leaching techniques (Berger et al., 2008; Fitzwater et al., 2003; Tang and Morel, 2006; Tovar-Sanchez et al., 2003), and assuming labile and refractory fractions represent biogenic and lithogenic fractions, respectively. A second approach is to use uptake ratios (metal/P) by phytoplankton to calculate the biogenic particulate metal concentrations, assuming that all P measured in bulk particles is biologically assimilated (i.e. lithogenic or authigenic P is negligible). The metal/P uptake ratios used in this approach come from uptake experiments using phytoplankton or from the slope of regression between dissolved metals and PO_4 in the upper ocean, assuming biological uptake is the main driver for variation in metal concentrations and nutrients (Liao et al., 2017; Planquette et al., 2013). In a similar fashion, this approach can also be used to estimate lithogenic metal concentrations, multiplying with crustal ratios (metal/Al or metal/Ti) with particulate Al or Ti concentrations in bulk particles (Liao et al., 2017; Little et al., 2016; Planquette et al., 2013) based on the assumption that all Al measured in bulk particles has a lithogenic origin and the used ratio is representative for all lithogenic particles.

Here, we compared the estimated biogenic and lithogenic metal concentrations and their relative contributions (percentage of each fraction relative to total metal concentration) to the bulk particle concentration in both the productive (the bloom stations) and less productive areas (Stns 53 and 52, here referred to as the non-bloom stations) using the two approaches described above – the first approach is referred to as the analytical leaching approach hereafter and the second approach is referred to as the fixed ratio approach hereafter. The concentrations and relative contributions are calculated by both approaches for each sample and summarized in depth intervals (depth-weighted averages for data in the bins, 0–50 m, 50–100 m, 100–200 m, 200–400 m, 400–600 m, 600–800 m, 800–1000 m, Fig. 11).

4.2.2.1. Biogenic metal concentration and relative contribution. For the analytical leaching approach, biogenic concentrations and contributions were derived from [LpMe] and [LpMe]/[TpMe], respectively, assuming LpMe is all biogenic. In the 0–50 m depth interval at the bloom stations, elevated biogenic [pZn] and [pCd] were estimated (1.22 ± 0.61 nmol L^{-1}; $n = 10$, and 0.14 ± 0.10 nmol L^{-1}; n = 10, mean ± 1 SD, respectively), and concentrations decreased with depth (Table 4, Fig. 11b and f). Similarly, a decreasing trend in biogenic pZn contributions from the surface (86%, 0–50 m) to greater depths (60%, 600–800 m) was calculated (Fig. 11a). As suggested by the relationship of TpP and TpZn (section 4.2.2), these results indicate a consistent and significant production of biogenic pZn in the surface of the ASP, as well as remineralization of biogenic pZn with depth. On the other hand, while biogenic [pCd] were also elevated within the 0–50 m layer compared to deeper depths at the bloom stations (Table 4 and Fig. 11f), the biogenic pCd contribution did not decrease significantly over depth (95–97%%, Fig. 11e). This indicates that biogenic pCd still dominates the particulate

Table 5
Compilation of Zn/P and Cd/P ratios, including both published values and this study. [dMe] denotes dissolved metal concentrations.

Field observations	Zn/P (mmol mol^{-1})	Cd/P (mmol mol^{-1})	Approach	Reference
The Amundsen Sea				
DIS bloom stations	3.94 ± 0.66	0.42 ± 0.06	slope of [dMe] and [PO_4] (the surface layer) (values for the "fixed ratio approach" in section 4.2.2.1)	this study
GIS bloom stations	2.74 ± 0.51	0.45 ± 0.08		
Non-bloom stations (st 52 & st. 53)	8.47 ± 0.73	0.60 ± 0.07		
DIS bloom stations (Haptophyte, 59–100%)	7.16 ± 0.40	0.64 ± 0.02	slope of [LpMe]/[LpP] (intercept: 0)	this study
GIS bloom stations (Diatoms, 54–91%%)	3.19 ± 0.30	0.48 ± 0.04		
Non-bloom stations (st 52 & st. 53)	11.6 ± 1.87	1.02 ± 0.10		
P. Antarctica	3.37		slope of [dMe] and [PO_4]	Sherrell et al., 2015
The Ross Sea				
P. Antarctica (74%)	7.7	0.65	calculated by the deficits compared to High Salinity Shelf Water (HSWW) for each nutrient in the mixed layer	Gerringa et al., 2020b
Diatom (88%)	3.7–4.0	0.54–0.57		
The Weddell Gyre				
Diatom (~80%)	6.36 ± 0.69	0.32	slope of [dMe] and [PO_4]	Viljoen et al., 2019
The Southern Ocean				
Diatom	11.1 ± 0.67	1.29 ± 0.07	bulk particles (Fe limited seawater)	Cullen et al., 2003
Average	6 ± 2.6	0.65 ± 0.3	slope of [dMe] and [PO_4]	Löscher, 1999; Ellwood, 2008; Lane et al., 2009; Saito et al., 2010; Croot et al., 2011
Culture experiments				
P. antarctica	n/a	0.20 ± 0.01 (Fe-deplete)		Lane et al., 2009
	n/a	0.042 ± 0.005 (Fe-replete)		
Diatom	8.1 (Fe-deplete)	n/a		Twining et al., 2004
	6.2 (Fe-replete)	n/a		

pool at depth, despite remineralization. At the non-bloom stations, lower biogenic [pZn] (0.86 ± 0.21 nmol L^{-1}) and biogenic [pCd] (0.08 ± 0.01 nmol L^{-1}) were estimated in the upper water layer (0–50 m) compared to the bloom stations, and both biogenic concentrations decreased with depth (Table 4). Lower biogenic metal concentrations at the non-bloom station suggests a relatively smaller biogenic particle production in the surface layer, coincident with lower fluorescence (Fig. 3c), likely due to the decreased availability of Fe compared to the bloom stations (van Manen et al., 2022). Interestingly, a higher percentage biogenic pZn contribution was estimated at 0–50 m at the non-bloom stations (96%) than at the bloom stations (86%), which implies less abiotic pZn at the non-bloom stations (further discussed in section 4.2.2.2). On the other hand, the biogenic pCd contribution was equally high (~97%) within 0–50 m at both bloom and non-bloom stations (Fig. 11e and g), suggesting abiotic pCd is not significant compared to biogenic pCd at both non-bloom and bloom stations.

In comparison to the analytical leaching approach, for the fixed ratio approach, we used TpP combined with the slope of regression between dissolved metals and phosphate in the surface layer (Table 5) as an estimation of the metal uptake ratios to estimate the biogenic concentration and relative contribution (Planquette et al., 2013; van Manen et al., 2022). The slope of regression was used as there is a lack of culture studies on metal and P uptake by haptophytes, and the difference in phytoplankton community between blooms may affect in-situ metal uptake ratios. Lower biogenic concentrations and contributions (LpMe/TpMe) were derived using this approach than with the analytical leaching approach (Fig. 11) – within all depth intervals, biogenic concentrations calculated by the analytical leaching approach are up to 5.1 times and up to 2.6 times higher than estimated by the fixed ratio approach for Zn and Cd, respectively (Fig. 11). That said, however, both approaches yielded a similar decreasing pattern of labile particulate concentrations of both metals from the surface to the deep.

A possible explanation for the discrepancy between these two commonly used approaches is that the ratios derived from the slope of the metal-phosphate relationships may not accurately represent the 'true' phytoplankton uptake ratios. Indeed, it is well established that care should be taken when assuming regression slopes are representative of uptake ratios, as such slopes may also be influenced by both water mass mixing and sources or sinks not associated with uptake and remineralization (e.g., Middag et al., 2019; Middag et al., 2018). Additionally, the uptake of metal and phosphate also differs between different phytoplankton species and under different environmental conditions (e.g., Ho et al., 2003), meaning that a universal slope of the dissolved metal-phosphate relationship may not represent the relevant actual uptake ratios. On the other hand, our definition of the 'labile' fraction might not necessarily equate to the biogenic fraction. For example, it has been found that labile pMe as defined by this leaching method can include not only metals from biogenic origin such as living organisms (soft tissue and hard skeletal materials such as calcite and aragonite) and biodetritus (e.g., dead phytoplankton cells, fecal pellets), but also metals associated with fresh authigenic particles (e.g., amorphous Fe-Mn oxyhydroxide), as well as metals weakly bound to lithogenic particles (e.g., alumino-silicate clay minerals or crystalline oxyhydroxide minerals) (Berger et al., 2008). Moreover, other sources of labile particles such as sediments that have different metal/*P* values, can result in variation in the observed ratios. Nevertheless, from this dataset, both approaches showed dominant biogenic contributions in the surface compared to the deep, indicating that the TpZn and TpCd pool in the surface of the ASP is mainly controlled by biological activity.

Overall, by comparing two different approaches, we found that there is no perfect approach to accurately determine the biogenic fraction – the estimation strongly depends on the chosen fixed ratios and the leaching selectiveness – in regions with high productivity and without significant input of other labile particulate sources, the analytical leaching approach could give representative results, although inherently there is a risk of including adsorbed/scavenged metals or authigenic

particles. On the other hand, the fixed ratio approach would be an ideal fit if the phytoplankton community and its uptake ratio during the development of blooms could be simultaneously monitored, rather than relying on estimates based on dissolved concentrations. Based on the data available in this study, we conclude that a variation of the 'analytical leaching' approach is most appropriate for assessing the metal uptake ratios in the biogenic fraction (see section 4.3).

4.2.2.2. Lithogenic metal concentration and relative contribution. To estimate the lithogenic concentration and contribution by the analytical leaching approach, it must be assumed that the RpMe fraction corresponds to the lithogenic fraction, whereas in the fixed ratio approach, the upper crustal metal/Al ratios (Zn/Al: 0.34 mmol mol^{-1}; Cd/Al: 0.45 μmol mol^{-1}, Rudnick and Gao, 2003) are used to derive lithogenic concentrations (based on TpAl) and contributions (lithogenic metals/TpMe).

In this section, since the ASP bloom stations are on the continental shelf (close to the coast), we refer to them as the coastal stations, whereas the non-bloom stations are referred to as the oceanic stations. Based on the analytical leaching approach, elevated lithogenic [pZn] were estimated at the coastal stations (75 ± 38 pmol L^{-1}, mean ± 1 SD) compared to the oceanic stations (17 ± 10 pmol L^{-1}) (though both are much lower than biogenic [pZn]) (Table 4). A similar elevation of lithogenic [pZn] at the coastal stations (18 ± 5 pmol L^{-1}) was estimated by the fixed ratio approach, compared to the oceanic stations (1.2 ± 0.7 pmol L^{-1}); both approaches thus indicate some lithogenic pZn input from the Antarctic continental shelf. In contrast, lithogenic [pCd] derived by the analytical leaching approach were very low and variable for both station groups (bloom stations: 0.95 ± 1.49 pmol L^{-1}; oceanic stations: 0.59 ± 0.91 pmol L^{-1}). For the fixed ratio approach, estimated lithogenic [pCd] were even lower at both station groups (< 0.03 pmol L^{-1}; Table 4), suggesting that the input of lithogenic pCd is negligible. Interestingly, the analytical leaching approach estimated higher coastal lithogenic concentrations in the surface (within 0–50 m) than in the deep (600–800 m) for both metals at both station groups (Table 4). We speculate that the surface elevation of lithogenic concentrations (derived by the analytical leaching approach) is likely affected by the high labile particle concentration in the surface layer where some LpMe is inevitably carried over refractory fraction, given that RpMe was very low and nearly 8 (for Zn) and 35 (for Cd) times lower than LpMe in the surface (Fig. 7).

The lithogenic pZn contribution at the coastal stations increased from the surface to depth estimated using both approaches – from 2% (0–50 m) to 18% (600–800 m) with the fixed ratio approach, and from 13% (0–50 m) to 40% (600–800 m) with the analytical leaching approach (Fig. 11). A similar pattern to the coastal stations was also observed at the oceanic stations. Taken together with decreasing biogenic [pZn] (and biogenic pZn contributions) with depth (Fig. 11), these findings are consistent with remineralization of biogenic particle with depth combined with an increasing (but relatively small) lithogenic input from shelf sediments.

4.3. Different uptake ratios (Zn/P and Cd/P) in the two sampling regions

As discussed in section 4.2.2, high biogenic particulate metals in the surface of the ASP were found corresponding with phytoplankton blooms. However, assessing the biogenic contribution to the particulate metal pool is complicated, with both the fixed ratio and the analytical leaching approach having caveats. Given that the blooms were dominated by different phytoplankton species, with haptophytes (typically *Phaeocystis* spp.) and diatoms dominating in the Dotson and the Getz regions, respectively (Fig. 6), the uptake of Zn and Cd would be expected to vary in the different blooms. Further, we would expect Zn and Cd uptake to vary during development of the bloom through time. As a result, we deem using the slopes of the regression between LpMe and

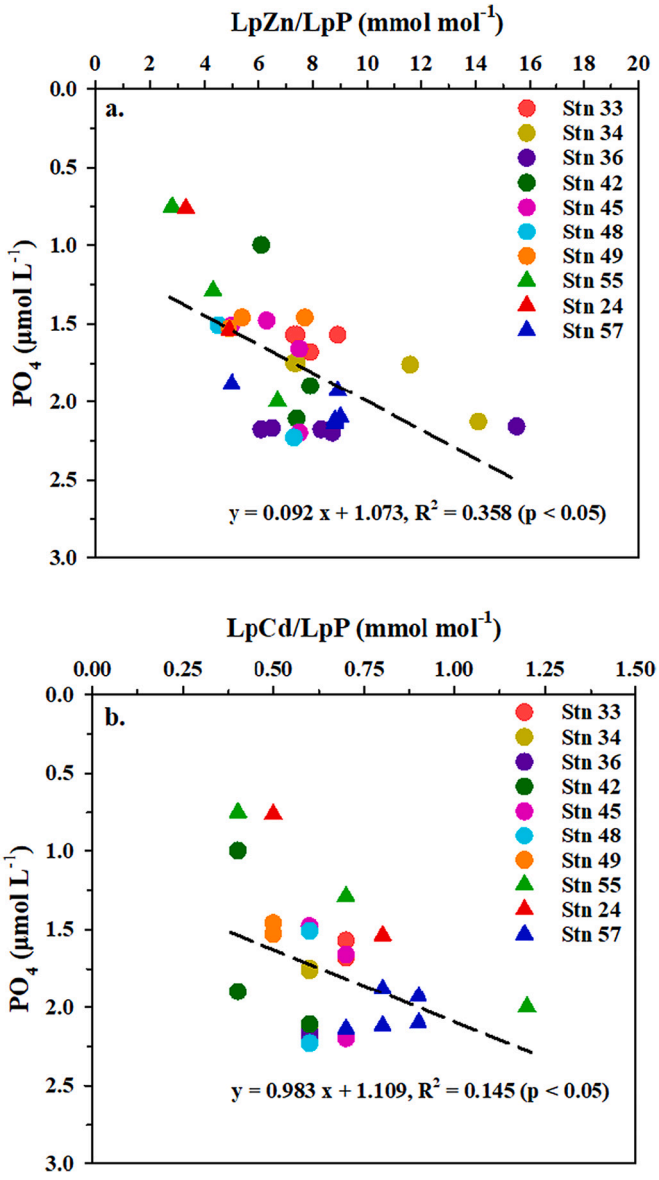

Fig. 12. Labile particulate composition (LpMe/LpP) versus dissolved PO_4 in the surface layer at the GPpr12 bloom stations. a. LpZn/LpP vs PO_4 b. LpCd/LpP vs PO_4. The black dash line represents the regression line.

labile pP (LpP) has the least underlying assumptions and may thus be more representative of true uptake than using either reported fixed ratios (fixed ratio approach) or individual (per sample) estimates from the analytical leaching approach. Hence, we used the slope of LpMe and LpP relationship (intercept set to 0, referred to as LpMe/LpP slope ratios hereafter) in the surface layer at the bloom stations to evaluate differences in uptake ratios of both metals.

Uptake of Cd by phytoplankton is thought to be related to Zn^{2+} availability, which also affects the uptake ratios of Zn. For example, Sunda and Huntsman (2000) reported increased Cd uptake relative to PO_4 by some oceanic diatoms (e.g., *Thalassiosira oceanica*) under Zn-depleted conditions (when [Zn^{2+}] decreased to 0.01 nmol L^{-1}). When dZn is depleted, Cd may substitute for Zn in some carbonic anhydrases, with some species even containing a Cd-based enzyme (Morel et al., 2020, and references therein). However, even though we have no estimates of [Zn^{2+}], [dZn] in the ASP is always relatively high (> 1 nmol L^{-1}), even in the surface layer where strong biological uptake occurs, implying relatively high [Zn^{2+}] as well (e.g., Baars and Croot, 2011). As such, it is unlikely that substitution effects play an important role in

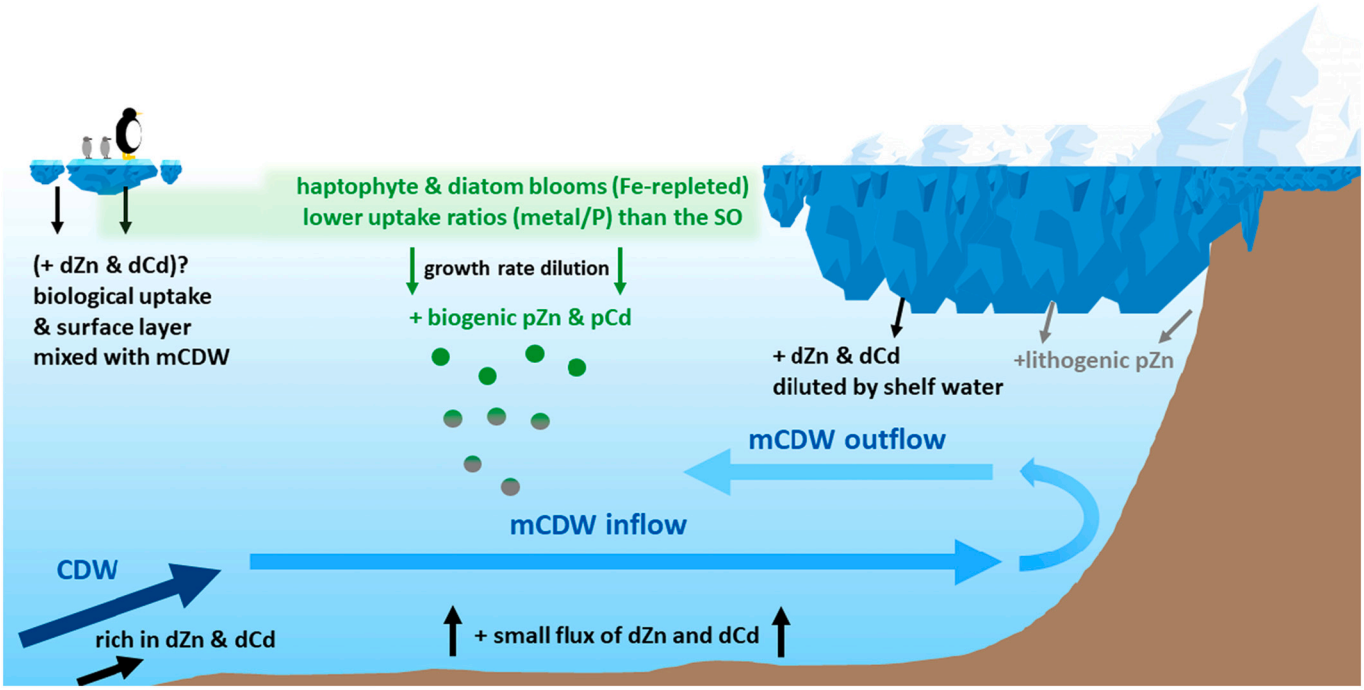

Fig. 13. Schematic of the sources and cycling of dissolved and particulate metals (Zn and Cd), as well as biogeochemical processes in the ASP. Blue arrows (from dark blue to light blue) represent the route of mCDW from the open SO to the ASP, modified by mixing with other water masses. Black and gray arrows indicate the sources of dMe and lithogenic pZn, respectively. Green arrows represent the production of biogenic pMe. Note: features are not to scale.

driving dCd uptake or Cd:P ratios in the ASP; indeed, no relationships between uptake ratios and dissolved metal concentrations were apparent in the current data that suggested a dominant role for substitution. Therefore, we do not focus on the interplay between Zn and Cd substitution in our discussion of the ASP.

We compared LpMe/LpP slope ratios with reported metal stoichiometric values for both *Phaeocystis antarctica* (*P. antarctica*) and Antarctic diatoms from published field observations in the Southern Ocean and coastal Antarctica, as well as from culture experiments (Table 5). In the diatom-dominated bloom, The LpZn/LpP (3.19 ± 0.30 mmol mol^{-1}) and LpCd/LpP (0.48 ± 0.04 mmol mol^{-1}) slope ratios were lower than previously reported in the Southern Ocean (Table 5). This variation is likely related to the availability of Fe as it has been suggested Fe replete conditions can increase the uptake of P relative to Zn and Cd ('growth rate dilution'; Cullen et al., 2003), and/or reduce Zn and Cd uptake through putative non-specific divalent metal transporters that are up-regulated under Fe-limitation condition (Kustka et al., 2007; Lane et al., 2008; Lane et al., 2009). Both mechanisms would result in higher uptake ratios of Zn and Cd relative to P in the Fe-depleted open Southern Ocean (de Baar et al., 1990; de Baar et al., 1999; Martin et al., 1990). The ASP is expected to be supplied by Fe from the melting of ice shelves and/or sea ice (Gerringa et al., 2012; Gerringa et al., 2020a; Sherrell et al., 2015; van Manen et al., 2022), as well as upwelling of Fe-rich deep water (Sherrell et al., 2015), which could lead to higher Fe supply. Indeed, for the non-bloom stations (Stns 53 and 52) where less phytoplankton biomass is observed (most likely due to less available Fe supply; van Manen et al., 2022), higher LpZn/LpP (11.6 ± 1.87 mmol mol^{-1}) and LpCd/LpP (1.02 ± 0.10 mmol mol^{-1}) slope ratios were calculated compared to both bloom stations (Table 5). This difference in LpMe/LpP slope ratios between the bloom stations and the non-bloom stations is consistent with the effect of Fe availability on Zn and Cd uptake in the ASP as suggested previously based on culture experiments (Twining et al., 2004) and shipboard incubations (Cullen et al., 2003; Table 5). Additionally, a significant regression was found between individual LpMe/LpP ratios (from the analytical leaching approach) and dissolved PO_4 (both $p < 0.05$) in the surface layer for the bloom stations. This relationship suggests that individual LpMe/LpP ratios decrease when phosphate decreases, indicating a growth rate dilution effect in the central ASP as lower PO_4 implies more growth (Fig. 12). In contrast, only a weak co-variance was observed for the non-bloom stations (for Zn: $R^2 = 0.45$; for Cd: $R^2 = 0.016$, both $p < 0.05$, not shown), most likely due to lower Fe supply and less phosphate uptake. A key finding from the observed variability in LpMe/LpP slope ratios is that uptake ratios could vary even over short distances or with depth in the ASP due to differences in Fe or light availability; such variation in uptake ratios has been suggested before (e.g., Alderkamp et al., 2015; Twining and Baines, 2013), but mainly as differences between geographical regions and between Fe-addition (culture) experiments. Our data suggest that (known) local gradients in Fe availability can indeed affect uptake ratios of Cd and Zn over short spatial scales in the ASP, notably between coastal and open ocean regions.

The LpZn/LpP (7.16 ± 0.40 mmol mol^{-1}) and LpCd/LpP (0.64 ± 0.02 mmol mol^{-1}) slope ratios observed in the haptophyte-dominated bloom are comparable to those found at a *P. antarctica*-dominated station in the Ross Sea (7.7 mmol mol^{-1} and 0.65 mmol mol^{-1} for Zn and Cd, respectively, Gerringa et al., 2020b), implying the haptophyte-dominated bloom could be *P. antarctica*-dominated. These ratios in the *P. antarctica*-dominated bloom are higher than in the diatom-dominated bloom, which suggests *P. antarctica* might have higher metal/P ratios than diatoms in Antarctic coastal waters. This result is different from previous studies that suggested diatoms have higher cellular metal/P ratios than *Phaeocystis* in the Southern Ocean (e.g., Twining and Baines, 2013). A potential explanation is that *Phaeocystis* regulates cellular nutrient (metal) requirements in adaptation to dynamic environmental conditions (e.g., McCain et al., 2022) – Sedwick et al. (2007) suggested that *Phaeocystis* lowers its Fe requirement under increasing irradiation enabling a longer bloom period in the Ross Sea. Since the interplay between the availability of Fe and light controls the development of phytoplankton blooms in the ASP (Park et al., 2017), we speculate that *P. antarctica* might increase their Zn and Cd uptake (relative to P) towards the end of the *P. antarctica*-dominated bloom period when Fe is scarce and growth rates are reduced, resulting in higher LpMe/LpP slope

ratios than estimated for diatoms in this study.

5. Conclusions

In this study we report the first combined dataset of dissolved and particulate Zn and Cd for the AS shelf region and the ASP. Our results highlight the dominant sources of both metals to the ASP and the importance of biological uptake and recycling for the particle composition of both metals. We conclude that inflowing CDW is the main source of dZn and dCd to the AS, with mCDW picking up a relatively small amount of additional dZn and sometimes dCd from shelf sediments (Fig. 13). However, ice shelf melt is not a significant source for either metal due to only a small melt water contribution and mixing with low metal shelf waters, whereas an assessment of the impact of sea ice on dissolved metal distributions was precluded by strong biological uptake in the surface layer. For particles, our data indicate that labile particulate metals are largely controlled by biogenic particle formation in the surface layer during the bloom period. We attribute refractory particulate Zn to resuspension of lithogenic particles from the shelf sediments and terrestrial material near the ice shelf. By contrast, however, no significant lithogenic source of particulate Cd was observed (Fig. 13). Relatively high biogenic particulate metal concentrations and contributions to the total particulate pool in surface waters were estimated to decrease over depth along both transects regardless of the used approach). Our estimated labile particulate metal/phosphate slope ratios in the diatom-dominated stations are much lower than those published for the open Southern Ocean, which may be linked to the relative availability of Fe in coastal Antarctic regions versus the open Southern Ocean that is often Fe-limited. Additionally, we observed different labile particulate metal/phosphate slope ratios between two different blooms in this study that were dominated by either haptophytes or diatoms respectively, implying these two phytoplankton groups might have different Zn, Cd, and P quotas in the biogeochemically dynamic ASP. Given that the volume of mCDW intruding onto the continental shelf is increasing as a result of global climate change (Jacobs et al., 2011; Mankoff et al., 2012), fluxes of dZn and dCd to the AS from both mCDW and benthic sources may increase. Enhanced mCDW inflow would be expected to increase nutrient (macronutrients as well as micronutrients including Fe) fluxes as well. Spatial and temporal variability in mCDW flow and trace metal sources will likely affect the productivity and biogeochemistry in the ASP (e.g., changes in uptake and uptake ratios of bio-available metals). Albeit regional, the findings of this study may have implications for the larger scale cycling of trace metals in the Southern Ocean and this should be further explored in future studies.

Declaration of Competing Interest

None.

Data availability

All dada is available via NIOZ data server (https://doi.org/10.25850/nioz/7b.b.bd).

Acknowledgment

This work was supported by funding (grant number: ALWPP.2016.020) from the Dutch Research Council (NWO), and T. Conway acknowledges support from National Science Foundation (NSF; USA) Award OCE2123354. Access to the region on the R/V Araon was provided by the Korea Polar Research institute (KOPRI). We acknowledge the captain and the crew of the R/V Araon, as well as all the scientists onboard, for their assistance and support during the expedition ANA08B (project number: PE21110). We also would like to thank Patrick Laan from the NIOZ trace metal team for his assistance with the trace metal measurements, and Dr. Willem van de Poll from the Faculty of Science and Engineering, University of Groningen, the Netherlands, for the assistance with the analysis of the phytoplankton composition, as well as Sven Ober and colleagues from NIOZ National Marine Facilities (NMF) for the preparation of the Titan sampling system and other facilities used during this expedition. Piet ter Schure and his team from DMT Marine Equipment are acknowledged for their great help with the winch setup for the Titan sampling system used on R/V Araon, as without their amazingly fast response to assemble a winch last minute, this research would not have been possible. Figs. 1 and 3 were derived using Python version 3.7.12, whereas Figs. 2, 4, 5, 7 and 8 were derived using ODV version 5.3.0 (Schlitzer, 2020), and Figs. 6, 9, 10 and 11 were derived using SigmaPlot version 14. The authors are grateful to the two reviewers and associate editor for their positive comments and constructive suggestions.

Appendix A. Supplementary data

Supplementary data to this article can be found online at https://doi.org/10.1016/j.marchem.2023.104223.

References

Abouchami, W., Galer, S.J.G., de Baar, H.J.W., Middag, R., Vance, D., Zhao, Y., Klunder, M., Mezger, K., Feldmann, H., Andreae, M.O., 2014. Biogeochemical cycling of cadmium isotopes in the Southern Ocean along the zero Meridian. Geochim. Cosmochim. Acta 127, 348–367.

Alderkamp, A.-C., Mills, M.M., van Dijken, G.L., Laan, P., Thuróczy, C.-E., Gerringa, L.J. A., de Baar, H.J.W., Payne, C.D., Visser, R.J.W., Buma, A.G.J., Arrigo, K.R., 2012. Iron from melting glaciers fuels phytoplankton blooms in the Amundsen Sea (Southern Ocean): phytoplankton characteristics and productivity. Deep-Sea Res. II Top. Stud. Oceanogr. 71-76, 32–48.

Alderkamp, A.-C., van Dijken, G.L., Lowry, K.E., Connelly, T.L., Lagerström, M., Sherrell, R.M., Haskins, C., Rogalsky, E., Schofield, O., Stammerjohn, S.E., Yager, P. L., Arrigo, K.R., 2015. Fe availability drives phytoplankton photosynthesis rates during spring bloom in the Amundsen Sea Polynya, Antarctica. Elementa: Sci. Anthropocene 3, 000043.

Anderson, P.S., 1993. Evidence for an Antarctic winter coastal polynya. Antarct. Sci. 5 (2), 221–226.

Ardelan, M.V., Holm-Hansen, O., Hewes, C.D., Reiss, C.S., Silva, N.S., Dulaiova, H., Steinnes, E., Sakshaug, E., 2010. Natural iron enrichment around the Antarctic peninsula in the Southern Ocean. Biogeosciences 7 (1), 11–25.

Arneborg, L., Wåhlin, A.K., Björk, G., Liljebladh, B., Orsi, A.H., 2012. Persistent inflow of warm water onto the Central Amundsen shelf. Nat. Geosci. 5 (12), 876–880.

Arrigo, K.R., van Dijken, G.L., 2003. Phytoplankton dynamics within 37 Antarctic coastal polynya systems. J. Geophys. Res. Oceans 108 (C8).

Arrigo, K.R., Worthen, D.L., Lizotte, M.P., Dixon, P., Dieckmann, G., 1997. Primary production in Antarctic Sea Ice. Science 276 (5311), 394.

Arrigo, K.R., Lowry, K.E., van Dijken, G.L., 2012. Annual changes in sea ice and phytoplankton in polynyas of the Amundsen Sea, Antarctica. Deep-Sea Res. II Top. Stud. Oceanogr. 71-76, 5–15.

Assmann, K.M., Jenkins, A., Shoosmith, D.R., Walker, D.P., Jacobs, S.S., Nicholls, K.W., 2013. Variability of circumpolar deep water transport onto the Amundsen Sea continental shelf through a shelf break trough. J. Geophys. Res. Oceans 118 (12), 6603–6620.

Baars, O., Croot, P.L., 2011. The speciation of dissolved zinc in the Atlantic sector of the Southern Ocean. Deep-Sea Res. II Top. Stud. Oceanogr. 58 (25), 2720–2732.

Baars, O., Abouchami, W., Galer, S.J.G., Boye, M., Croot, P.L., 2014. Dissolved cadmium in the Southern Ocean: distribution, speciation, and relation to phosphate. Limnol. Oceanogr. 59 (2), 385–399.

Berger, C.J.M., Lippiatt, S.M., Lawrence, M.G., Bruland, K.W., 2008. Application of a chemical leach technique for estimating labile particulate aluminum, iron, and manganese in the Columbia River plume and coastal waters off Oregon and Washington. J. Geophys. Res. Oceans 113 (C2).

Biller, D.V., Bruland, K.W., 2012. Analysis of Mn, Fe, Co, Ni, Cu, Zn, Cd, and Pb in seawater using the Nobias-chelate PA1 resin and magnetic sector inductively coupled plasma mass spectrometry (ICP-MS). Mar. Chem. 130-131, 12–20.

Boyle, E.A., 1988. Cadmium: chemical tracer of Deepwater paleoceanography. Paleoceanography 3 (4), 471–489.

Boyle, E.A., Huested, S.S., Jones, S.P., 1981. On the distribution of copper, nickel, and cadmium in the surface waters of the North Atlantic and North Pacific Ocean. J. Geophys. Res. Oceans 86 (C9), 8048–8066.

Bruland, K.W., 1980. Oceanographic distributions of cadmium, zinc, nickel, and copper in the North Pacific. Earth Planet. Sci. Lett. 47 (2), 176–198.

Bruland, K.W., Donat, J.R., Hutchins, D.A., 1991. Interactive influences of bioactive trace metals on biological production in oceanic waters. Limnol. Oceanogr. 36 (8), 1555–1577.

Bruland, K.W., Middag, R., Lohan, M.C., 2013. Controls of trace metals in seawater. In: Mottl, M.J., Elderfield, H. (Eds.), Treatise on Geochemistry, Second edition. Saunders, Elsevier Inc, Philadelphia, USA, pp. 19–51.

Connolley, W.M., 1997. Variability in annual mean circulation in southern high latitudes. Clim. Dyn. 13 (10), 745–756.
Conway, T.M., John, S.G., 2014. The biogeochemical cycling of zinc and zinc isotopes in the North Atlantic Ocean. Glob. Biogeochem. Cycles 28 (10), 1111–1128.
Croft, M.T., Lawrence, A.D., Raux-Deery, E., Warren, M.J., Smith, A.G., 2005. Algae acquire vitamin B12 through a symbiotic relationship with bacteria. Nature 438 (7064), 90–93.
Croot, P.L., Baars, O., Streu, P., 2011. The distribution of dissolved zinc in the Atlantic sector of the Southern Ocean. Deep-Sea Res. II Top. Stud. Oceanogr. 58 (25), 2707–2719.
Cullen, J.T., 2006. On the nonlinear relationship between dissolved cadmium and phosphate in the modern global ocean: could chronic iron limitation of phytoplankton growth cause the kink? Limnol. Oceanogr. 51 (3), 1369–1380.
Cullen, J.T., Chase, Z., Coale, K.H., Fitzwater, S.E., Sherrell, R.M., 2003. Effect of iron limitation on the cadmium to phosphorus ratio of natural phytoplankton assemblages from the Southern Ocean. Limnol. Oceanogr. 48 (3), 1079–1087.
de Baar, H.J.W., Buma, A.G.J., Nolting, R.F., Cadée, G.C., Jacques, G., Tréguer, P.J., 1990. On iron limitation of the Southern Ocean: experimental observations in the Weddell and scotia seas. Mar. Ecol. Prog. Ser. 65 (2), 105–122.
de Baar, H.J.W., Saager, P.M., Nolting, R.F., van der Meer, J., 1994. Cadmium versus phosphate in the world ocean. Mar. Chem. 46 (3), 261–281.
de Baar, H.J.W., de Jong, J.T.M., Nolting, R.F., Timmermans, K.R., van Leeuwe, M.A., Bathmann, U., Rutgers van der Loeff, M., Sildam, J., 1999. Low dissolved Fe and the absence of diatom blooms in remote Pacific waters of the Southern Ocean. Mar. Chem. 66 (1), 1–34.
de Baar, H.J.W., Timmermans, K.R., Laan, P., De Porto, H.H., Ober, S., Blom, J.J., Bakker, M.C., Schilling, J., Sarthou, G., Smit, M.G., Klunder, M., 2008. Titan: a new facility for ultraclean sampling of trace elements and isotopes in the deep oceans in the international Geotraces program. Mar. Chem. 111 (1), 4–21.
de Souza, G.F., Khatiwala, S.P., Hain, M.P., Little, S.H., Vance, D., 2018. On the origin of the marine zinc–silicon correlation. Earth Planet. Sci. Lett. 492, 22–34.
Duprat, L., Corkill, M., Genovese, C., Townsend, A.T., Moreau, S., Meiners, K.M., Lannuzel, D., 2020. Nutrient distribution in East Antarctic summer sea ice: a potential iron contribution from glacial basal melt. J. Geophys. Res. Oceans 125 (12), e2020JC016130.
Dutrieux, P., De Rydt, J., Jenkins, A., Holland, P.R., Ha, H.K., Lee, S.H., Steig, E.J., Ding, Q., Abrahamsen, E.P., Schröder, M., 2014. Strong sensitivity of Pine Island ice-shelf melting to climatic variability. Science 343 (6167), 174.
Eich, C., Biggs, T.E.G., van de Poll, W.H., van Manen, M., Tian, H.-A., Jung, J., Lee, Y., Middag, R., Brussaard, C.P.D., 2022. Ecological Importance of Viral Lysis as a Loss Factor of Phytoplankton in the Amundsen Sea. Microorganisms 10 (10):1967.
Ellwood, M.J., 2008. Wintertime trace metal (Zn, Cu, Ni, Cd, Pb and Co) and nutrient distributions in the Subantarctic zone between 40–52°S; 155–160°E. Mar. Chem. 112 (1), 107–117.
Fan, S., Gao, Y., Sherrell, R.M., Yu, S., Bu, K., 2021. Concentrations, particle-size distributions, and dry deposition fluxes of aerosol trace elements over the Antarctic peninsula in austral summer. Atmos. Chem. Phys. 21 (3), 2105–2124.
Fitzwater, S.E., Johnson, K.S., Elrod, V.A., Ryan, J.P., Coletti, L.J., Tanner, S.J., Gordon, R.M., Chavez, F.P., 2003. Iron, nutrient and phytoplankton biomass relationships in upwelled waters of the California coastal system. Cont. Shelf Res. 23 (16), 1523–1544.
George, E., Stirling, C.H., Gault-Ringold, M., Ellwood, M.J., Middag, R., 2019. Marine biogeochemical cycling of cadmium and cadmium isotopes in the extreme nutrient-depleted subtropical gyre of the South West Pacific Ocean. Earth Planet. Sci. Lett. 514, 84–95.
Gerringa, L.J.A., Alderkamp, A.-C., Laan, P., Thuróczy, C.-E., De Baar, H.J.W., Mills, M. M., van Dijken, G.L., Haren, H.V., Arrigo, K.R., 2012. Iron from melting glaciers fuels the phytoplankton blooms in Amundsen Sea (Southern Ocean): Iron biogeochemistry. Deep-Sea Res. II Top. Stud. Oceanogr. 71-76, 16–31.
Gerringa, L.J.A., Alderkamp, A.-C., Laan, P., Thuróczy, C.-E., De Baar, H.J.W., Mills, M. M., van Dijken, G.L., Haren, H.V., Arrigo, K.R., 2020a. Corrigendum to "Iron from melting glaciers fuels the phytoplankton blooms in Amundsen Sea (Southern Ocean): iron biogeochemistry" (Gerringa et al., 2012). Deep-Sea Res. II Top. Stud. Oceanogr. 177, 104843.
Gerringa, L.J.A., Alderkamp, A.-C., van Dijken, G., Laan, P., Middag, R., Arrigo, K.R., 2020b. Dissolved trace metals in the Ross Sea. Front. Mar. Sci. 7, 874.
Gordon, L.I., Jennings, J.C., Ross, A.A., 2001. A Suggested Protocol for Continuous Flow Automated Analysis of Seawater Nutrients Using the Alpkem Flow Solution IV System (Phosphate, Nitrate, Nitrite, Silicic Acid and Ammonia) chemical protocols used in the WOCE Hydrographic Program and the Joint Global Ocean Fluxes Study.
Gourmelen, N., Goldberg, D.N., Snow, K., Henley, S.F., Bingham, R.G., Kimura, S., Hogg, A.E., Shepherd, A., Mouginot, J., Lenaerts, J.T.M., Ligtenberg, S.R.M., van de Berg, W.J., 2017. Channelized melting drives thinning under a rapidly melting Antarctic ice shelf. Geophys. Res. Lett. 44 (19), 9796–9804.
Ha, H.K., Wåhlin, A.K., Kim, T.W., Lee, S.H., Lee, J.H., Lee, H.J., Hong, C.S., Arneborg, L., Björk, G., Kalén, O., 2014. Circulation and modification of warm deep water on the Central Amundsen shelf. J. Phys. Oceanogr. 44 (5), 1493–1501.
Henley, S.F., Cavan, E.L., Fawcett, S.E., Kerr, R., Monteiro, T., Sherrell, R.M., Bowie, A. R., Boyd, P.W., Barnes, D.K.A., Schloss, I.R., Marshall, T., Flynn, R., Smith, S., 2020. Changing biogeochemistry of the Southern Ocean and its ecosystem implications. Front. Mar. Sci. 7.
Herraiz-Borreguero, L., Lannuzel, D., van der Merwe, P., Treverrow, A., Pedro, J.B., 2016. Large flux of iron from the Amery Ice Shelf marine ice to Prydz Bay, East Antarctica. J. Geophys. Res. Oceans 121 (8), 6009–6020.
Ho, T.-Y., Quigg, A., Finkel, Z.V., Milligan, A.J., Wyman, K., Falkowski, P.G., Morel, F.M. M., 2003. The elemental composition of some marine phytoplankton1. J. Phycol. 39 (6), 1145–1159.
Hosking, J.S., Orr, A., Marshall, G.J., Turner, J., Phillips, T., 2013. The Influence of the Amundsen–Bellingshausen Seas Low on the Climate of West Antarctica and Its Representation in Coupled Climate Model Simulations. J. Clim. 26 (17), 6633–6648.
Jacobs, S.S., Hellmer, H.H., Jenkins, A., 1996. Antarctic ice sheet melting in the Southeast Pacific. Geophys. Res. Lett. 23 (9), 957–960.
Jacobs, S.S., Jenkins, A., Giulivi, C.F., Dutrieux, P., 2011. Stronger ocean circulation and increased melting under Pine Island Glacier ice shelf. Nat. Geosci. 4 (8), 519–523.
Jacobs, S., Jenkins, A., Hellmer, H., Giulivi, C., Nitsche, F., Huber, B., Guerrero, R., 2012. The Amundsen Sea and the Antarctic ice sheet. Oceanography 25 (3), 154–163.
Jenkins, A., Dutrieux, P., Jacobs, S.S., McPhail, S.D., Perrett, J.R., Webb, A.T., White, D., 2010. Observations beneath Pine Island Glacier in West Antarctica and implications for its retreat. Nat. Geosci. 3 (7), 468–472.
Jeon, M.H., Jung, J., Park, M.O., Aoki, S., Kim, T.-W., Kim, S.-K., 2021. Tracing circumpolar deep water and glacial meltwater using humic-like fluorescent dissolved organic matter in the Amundsen Se, Antarcticaa. Mar. Chem. 235, 104008.
Johnson, K.S., Elrod, V., Fitzwater, S., Plant, J., Boyle, E., Bergquist, B., Bruland, K., Aguilar-Islas, A., Buck, K., Lohan, M., Smith, G.J., Sohst, B., Coale, K., Gordon, M., Tanner, S., Measures, C., Moffett, J., Barbeau, K., King, A., Bowie, A., Chase, Z., Cullen, J., Laan, P., Landing, W., Mendez, J., Milne, A., Obata, H., Doi, T., Ossiander, L., Sarthou, G., Sedwick, P., Van den Berg, S., Laglera-Baquer, L., Wu, J.-F., Cai, Y., 2007. Developing standards for dissolved iron in seawater. EOS Trans. Am. Geophys. Union 88 (11), 131–132.
Kellogg, M.M., McIlvin, M.R., Vedamati, J., Twining, B.S., Moffett, J.W., Marchetti, A., Moran, D.M., Saito, M.A., 2020. Efficient zinc/cobalt inter-replacement in Northeast Pacific diatoms and relationship to high surface dissolved Co : Zn ratios. Limnol. Oceanogr. 65 (11), 2557–2582.
Kim, T.W., Ha, H.K., Wåhlin, A.K., Lee, S.H., Kim, C.S., Lee, J.H., Cho, Y.K., 2017. Is Ekman pumping responsible for the seasonal variation of warm circumpolar deep water in the Amundsen Sea? Cont. Shelf Res. 132, 38–48.
Kim, T.-W., Yang, H.W., Dutrieux, P., Wåhlin, A.K., Jenkins, A., Kim, Y.G., Ha, H.K., Kim, C.-S., Cho, K.-H., Park, T., Park, J., Lee, S., Cho, Y.-K., 2021. Interannual variation of modified circumpolar deep water in the Dotson-Getz trough, West Antarctica. J. Geophys. Res. Oceans 126 (12), e2021JC017491.
Kustka, A.B., Allen, A.E., Morel, F.M.M., 2007. Sequence analysis and transcriptional regulation of iron acquisition genes in two marine diatoms. J. Phycol. 43 (4), 715–729.
Lane, E.S., Jang, K., Cullen, J.T., Maldonado, M.T., 2008. The interaction between inorganic iron and cadmium uptake in the marine diatom Thalassiosira oceanica. Limnol. Oceanogr. 53 (5), 1784–1789.
Lane, E.S., Semeniuk, D.M., Strzepek, R.F., Cullen, J.T., Maldonado, M.T., 2009. Effects of iron limitation on intracellular cadmium of cultured phytoplankton: implications for surface dissolved cadmium to phosphate ratios. Mar. Chem. 115 (3), 155–162.
Lannuzel, D., Schoemann, V., de Jong, J., Tison, J.-L., Chou, L., 2007. Distribution and biogeochemical behaviour of iron in the East Antarctic Sea ice. Mar. Chem. 106 (1), 18–32.
Lannuzel, D., Schoemann, V., de Jong, J., Chou, L., Delille, B., Becquevort, S., Tison, J.-L., 2008. Iron study during a time series in the western Weddell pack ice. Mar. Chem. 108 (1), 85–95.
Lannuzel, D., Schoemann, V., de Jong, J., Pasquer, B., van der Merwe, P., Masson, F., Tison, J.-L., Bowie, A., 2010. Distribution of dissolved iron in Antarctic Sea ice: spatial, seasonal, and inter-annual variability. J. Geophys. Res. Biogeosci. 115 (G3).
Lannuzel, D., Bowie, A.R., van der Merwe, P.C., Townsend, A.T., Schoemann, V., 2011. Distribution of dissolved and particulate metals in Antarctic Sea ice. Mar. Chem. 124 (1), 134–146.
Lemaitre, N., de Souza, G.F., Archer, C., Wang, R.-M., Planquette, H., Sarthou, G., Vance, D., 2020. Pervasive sources of isotopically light zinc in the North Atlantic Ocean. Earth Planet. Sci. Lett. 539, 116216.
Li, F., Ginoux, P., Ramaswamy, V., 2008. Distribution, transport, and deposition of mineral dust in the Southern Ocean and Antarctica: contribution of major sources. J. Geophys. Res.-Atmos. 113 (D10).
Liao, W.-H., Yang, S.-C., Ho, T.-Y., 2017. Trace metal composition of size-fractionated plankton in the Western Philippine Sea: the impact of anthropogenic aerosol deposition. Limnol. Oceanogr. 62 (5), 2243–2259.
Liao, W.-H., Takano, S., Yang, S.-C., Huang, K.-F., Sohrin, Y., Ho, T.-Y., 2020. Zn isotope composition in the water column of the northwestern Pacific Ocean: the importance of external sources. Glob. Biogeochem. Cycles 34 (1), e2019GB006379.
Little, S.H., Vance, D., McManus, J., Severmann, S., 2016. Key role of continental margin sediments in the oceanic mass balance of Zn and Zn isotopes. Geology 44 (3), 207–210.
Lohan, M.C., Statham, P.J., Crawford, D.W., 2002. Total dissolved zinc in the upper water column of the subarctic North East Pacific. Deep-Sea Res. II Top. Stud. Oceanogr. 49 (24), 5793–5808.
Löscher, B.M., 1999. Relationships among Ni, Cu, Zn, and major nutrients in the Southern Ocean. Mar. Chem. 67 (1), 67–102.
Mackey, M.D., Mackey, D.J., Higgins, H.W., Wright, S.W., 1996. CHEMTAX - a program for estimating class abundances from chemical markers: application to HPLC measurements of phytoplankton. Mar. Ecol. Prog. Ser. 144, 265–283.
Mahowald, N.M., Hamilton, D.S., Mackey, K.R.M., Moore, J.K., Baker, A.R., Scanza, R.A., Zhang, Y., 2018. Aerosol trace metal leaching and impacts on marine microorganisms. Nat. Commun. 9 (1), 2614.
Mankoff, K.D., Jacobs, S.S., Tulaczyk, S.M., Stammerjohn, S.E., 2012. The role of Pine Island Glacier ice shelf basal channels in deep-water upwelling, polynyas and ocean circulation in Pine Island Bay, Antarctica. Ann. Glaciol. 53 (60), 123–128.

Marsay, C.M., Kadko, D., Landing, W.M., Morton, P.L., Summers, B.A., Buck, C.S., 2018. Concentrations, provenance and flux of aerosol trace elements during US GEOTRACES Western Arctic cruise GN01. Chem. Geol. 502, 1–14.
Martin, J.H., Fitzwater, S.E., Gordon, R.M., 1990. Iron deficiency limits phytoplankton growth in Antarctic waters. Glob. Biogeochem. Cycles 4 (1), 5–12.
McCain, J.S.P., Allen, A.E., Bertrand, E.M., 2022. Proteomic traits vary across taxa in a coastal Antarctic phytoplankton bloom. ISME J. 16 (2), 569–579.
Meredith, M.P., Venables, H.J., Clarke, A., Ducklow, H.W., Erickson, M., Leng, M.J., Lenaerts, J.T.M., van den Broeke, M.R., 2013. The freshwater system west of the Antarctic peninsula: spatial and temporal changes. J. Clim. 26 (5), 1669–1684.
Middag, R., van Heuven, S.M.A.C., Bruland, K.W., de Baar, H.J.W., 2018. The relationship between cadmium and phosphate in the Atlantic Ocean unravelled. Earth Planet. Sci. Lett. 492, 79–88.
Middag, R., de Baar, H.J.W., Bruland, K.W., 2019. The relationships between dissolved zinc and major nutrients phosphate and silicate along the GEOTRACES GA02 transect in the West Atlantic Ocean. Glob. Biogeochem. Cycles 33 (1), 63–84.
Miles, T., Lee, S.H., Wåhlin, A., Ha, H.K., Kim, T.W., Assmann, K.M., Schofield, O., 2016. Glider observations of the Dotson Ice Shelf outflow. Deep-Sea Res. II Top. Stud. Oceanogr. 123, 16–29.
Moreau, S., Lannuzel, D., Janssens, J., Arroyo, M.C., Corkill, M., Cougnon, E., Genovese, C., Legresy, B., Lenton, A., Puigcorbé, V., Ratnarajah, L., Rintoul, S., Roca-Martí, M., Rosenberg, M., Shadwick, E.H., Silvano, A., Strutton, P.G., Tilbrook, B., 2019. Sea ice meltwater and circumpolar deep water drive contrasting productivity in three Antarctic polynyas. J. Geophys. Res. Oceans 124 (5), 2943–2968.
Morel, F.M.M., Price, N.M., 2003. The biogeochemical cycles of trace metals in the oceans. Science 300 (5621), 944.
Morel, F.M.M., Reinfelder, J.R., Roberts, S.B., Chamberlain, C.P., Lee, J.G., Yee, D., 1994. Zinc and carbon co-limitation of marine phytoplankton. Nature 369 (6483), 740–742.
Morel, F.M.M., Lam, P.J., Saito, M.A., 2020. Trace metal substitution in marine phytoplankton. Annu. Rev. Earth Planet. Sci. 48 (1), 491–517.
Mu, L., Stammerjohn, S.E., Lowry, K.E., Yager, P.L., 2014. Spatial variability of surface pCO2 and air-sea CO2 flux in the Amundsen Sea polynya, Antarctica. Elementa: Sci. Anthropocene 3, 000036.
Nakamura, K., Aoki, S., Yoshimura, K., Kurita, N., 2014. Distribution of oxygen isotope ratio of precipitation in the Atlantic-Indian sectors of the Southern Ocean. SOLA 10, 154–157.
Ohnemus, D.C., Auro, M.E., Sherrell, R.M., Lagerström, M., Morton, P.L., Twining, B.S., Rauschenberg, S., Lam, P.J., 2014. Laboratory intercomparison of marine particulate digestions including piranha: a novel chemical method for dissolution of polyethersulfone filters. Limnol. Oceanogr. Methods 12 (8), 530–547.
Östlund, H.G., Hut, G., 1984. Arctic Ocean water mass balance from isotope data. J. Geophys. Res. Oceans 89 (C4), 6373–6381.
Park, J., Kuzminov, F.I., Bailleul, B., Yang, E.J., Lee, S., Falkowski, P.G., Gorbunov, M.Y., 2017. Light availability rather than Fe controls the magnitude of massive phytoplankton bloom in the Amundsen Sea polynyas, Antarctica. Limnol. Oceanogr. 62 (5), 2260–2276.
Pease, C.H., 1987. The size of wind-driven coastal polynyas. J. Geophys. Res. Oceans 92 (C7), 7049–7059.
Planquette, H., Sherrell, R.M., 2012. Sampling for particulate trace element determination using water sampling bottles: methodology and comparison to in situ pumps. Limnol. Oceanogr. Methods 10 (5), 367–388.
Planquette, H., Sherrell, R.M., Stammerjohn, S., Field, M.P., 2013. Particulate iron delivery to the water column of the Amundsen Sea, Antarctica. Mar. Chem. 153, 15–30.
Raiswell, R., Hawkings, J.R., Benning, L.G., Baker, A.R., Death, R., Albani, S., Mahowald, N., Krom, M.D., Poulton, S.W., Wadham, J., Tranter, M., 2016. Potentially bioavailable iron delivery by iceberg-hosted sediments and atmospheric dust to the polar oceans. Biogeosciences 13 (13), 3887–3900.
Randall-Goodwin, Meredith, M.P., Jenkins, A., Yager, P., Sherrell, R.M., Abrahamsen, E. P., Guerrero, R., Yuan, X., Mortlock, R.A., Gavahan, K., Alderkamp, A.-C., Ducklow, H., Robertson, R., Stammerjohn, S.E., 2015. Freshwater distributions and water mass structure in the Amundsen Sea Polynya region, Antarctica. Elementa: Sci. Anthropocene 3, 000065.
Rauschenberg, S., Twining, B.S., 2015. Evaluation of approaches to estimate biogenic particulate trace metals in the ocean. Mar. Chem. 171, 67–77.
Rignot, E., Bamber, J.L., van den Broeke, M.R., Davis, C., Li, Y., van de Berg, W.J., van Meijgaard, E., 2008. Recent Antarctic ice mass loss from radar interferometry and regional climate modelling. Nat. Geosci. 1 (2), 106–110.
Rijkenberg, M.J.A., de Baar, H.J.W., Bakker, K., Gerringa, L.J.A., Keijzer, E., Laan, M., Laan, P., Middag, R., Ober, S., van Ooijen, J., Ossebaar, S., van Weerlee, E.M., Smit, M.G., 2015. "PRISTINE", a new high volume sampler for ultraclean sampling of trace metals and isotopes. Mar. Chem. 177, 501–509.
Rudnick, R.L., Gao, S., 2003. Composition of the continental crust. In: Holland, H.D., Rudnick, R.L., Turekian, K.K. (Eds.), The Crust. Elsevier-Pergamon, Oxford, UK.
Saito, M.A., Goepfert, T.J., Ritt, J.T., 2008. Some thoughts on the concept of colimitation: three definitions and the importance of bioavailability. Limnol. Oceanogr. 53 (1), 276–290.
Saito, M.A., Goepfert, T.J., Noble, A.E., Bertrand, E.M., Sedwick, P.N., DiTullio, G.R., 2010. A seasonal study of dissolved cobalt in the Ross Sea, Antarctica: micronutrient behavior, absence of scavenging, and relationships with Zn, cd, and P. Biogeosciences 7 (12), 4059–4082.
Schlitzer, R., 2020. Ocean Data View.
Schmitt, A.-D., Galer, S.J.G., Abouchami, W., 2009. Mass-dependent cadmium isotopic variations in nature with emphasis on the marine environment. Earth Planet. Sci. Lett. 277 (1), 262–272.
Sedwick, P.N., DiTullio, G.R., 1997. Regulation of algal blooms in Antarctic shelf waters by the release of iron from melting sea ice. Geophys. Res. Lett. 24 (20), 2515–2518.
Sedwick, P.N., Garcia, N.S., Riseman, S.F., Marsay, C.M., DiTullio, G.R., 2007. Evidence for high iron requirements of colonial Phaeocystis antarctica at low irradiance. In: van Leeuwe, M.A., Stefels, J., Belviso, S., Lancelot, C., Verity, P.G., Gieskes, W.W.C. (Eds.), Phaeocystis, Major Link in the Biogeochemical Cycling of Climate-Relevant Elements. Springer, Netherlands, Dordrecht, pp. 83–97.
Selz, V., Lowry, K.E., Lewis, K.M., Joy-Warren, H.L., Poll, W., Nirmel, S., Tong, A., Arrigo, K.R., 2018. Distribution of Phaeocystis antarctica-dominated sea ice algal communities and their potential to seed phytoplankton across the western Antarctic Peninsula in spring. Mar. Ecol. Prog. Ser. 586, 91–112.
Shepherd, A., Wingham, D., Rignot, E., 2004. Warm ocean is eroding West Antarctic ice sheet. Geophys. Res. Lett. 31 (23).
Shepherd, A., Ivins, E.R., A, G., Barletta, V.R., Bentley, M.J., Bettadpur, S., Briggs, K.H., Bromwich, D.H., Forsberg, R., Galin, N., Horwath, M., Jacobs, S., Joughin, I., King, M.A., Lenaerts, J.T.M., Li, J., Ligtenberg, S.R.M., Luckman, A., Luthcke, S.B., McMillan, M., Meister, R., Milne, G., Mouginot, J., Muir, A., Nicolas, J.P., Paden, J., Payne, A.J., Pritchard, H., Rignot, E., Rott, H., Sørensen, L.S., Scambos, T.A., Scheuchl, B., Schrama, E.J.O., Smith, B., Sundal, A.V., van Angelen, J.H., van de Berg, W.J., van den Broeke, M.R., Vaughan, D.G., Velicogna, I., Wahr, J., Whitehouse, P.L., Wingham, D.J., Yi, D., Young, D., Zwally, H.J., 2012. A reconciled estimate of ice-sheet mass balance. Science 338 (6111), 1183.
Sherrell, R.M., Lagerström, M.E., Forsch, K.O., Stammerjohn, S.E., Yager, P.L., 2015. Dynamics of dissolved iron and other bioactive trace metals (Mn, Ni, Cu, Zn) in the Amundsen Sea Polynya, Antarctica. Elementa: Sci. Anthropocene 3, 000071.
Sieber, M., Conway, T.M., de Souza, G.F., Hassler, C.S., Ellwood, M.J., Vance, D., 2019. High-resolution Cd isotope systematics in multiple zones of the Southern Ocean from the Antarctic circumnavigation expedition. Earth Planet. Sci. Lett. 527, 115799.
Sieber, M., Conway, T.M., de Souza, G.F., Hassler, C.S., Ellwood, M.J., Vance, D., 2020. Cycling of zinc and its isotopes across multiple zones of the Southern Ocean: insights from the Antarctic circumnavigation expedition. Geochim. Cosmochim. Acta 268, 310–324.
Smith Jr., W.O., Comiso, J.C., 2008. Influence of sea ice on primary production in the Southern Ocean: A satellite perspective. J. Geophys. Res. Oceans 113 (C5).
Smith Jr., W.O., Gordon, L.I., 1997. Hyperproductivity of the Ross Sea (Antarctica) polynya during austral spring. Geophys. Res. Lett. 24 (3), 233–236.
St-Laurent, P., Yager, P.L., Sherrell, R.M., Stammerjohn, S.E., Dinniman, M.S., 2017. Pathways and supply of dissolved iron in the Amundsen Sea (Antarctica). J. Geophys. Res. Oceans 122 (9), 7135–7162.
Sunda, W.G., Huntsman, S.A., 1995. Cobalt and zinc interreplacement in marine phytoplankton: biological and geochemical implications. Limnol. Oceanogr. 40 (8), 1404–1417.
Sunda, W.G., Huntsman, S.A., 1998. Interactions among Cu2+, Zn2+, and Mn2+ in controlling cellular Mn, Zn, and growth rate in the coastal alga Chlamydomonas. Limnol. Oceanogr. 43 (6), 1055–1064.
Sunda, W.G., Huntsman, S.A., 2000. Effect of Zn, Mn, and Fe on Cd accumulation in phytoplankton: implications for oceanic Cd cycling. Limnol. Oceanogr. 45 (7), 1501–1516.
Sunda, W.G., Huntsman, S.A., 2005. Effect of CO2 supply and demand on zinc uptake and growth limitation in a coastal diatom. Limnol. Oceanogr. 50 (4), 1181–1192.
Tang, D., Morel, F.M.M., 2006. Distinguishing between cellular and Fe-oxide-associated trace elements in phytoplankton. Mar. Chem. 98 (1), 18–30.
Thoma, M., Jenkins, A., Holland, D., Jacobs, S., 2008. Modelling circumpolar deep water intrusions on the Amundsen Sea continental shelf, Antarctica. Geophys. Res. Lett. 35 (18).
Tovar-Sanchez, A., Sañudo-Wilhelmy, S.A., Garcia-Vargas, M., Weaver, R.S., Popels, L.C., Hutchins, D.A., 2003. A trace metal clean reagent to remove surface-bound iron from marine phytoplankton. Mar. Chem. 82 (1), 91–99.
Tovar-Sánchez, A., Duarte, C.M., Alonso, J.C., Lacorte, S., Tauler, R., Galbán-Malagón, C., 2010. Impacts of metals and nutrients released from melting multiyear Arctic Sea ice. J. Geophys. Res. Oceans 115 (C7).
Twining, B.S., Baines, S.B., 2013. The trace metal composition of marine phytoplankton. Annu. Rev. Mar. Sci. 5 (1), 191–215.
Twining, B.S., Baines, S.B., Fisher, N.S., 2004. Element stoichiometries of individual plankton cells collected during the Southern Ocean iron experiment (SOFeX). Limnol. Oceanogr. 49 (6), 2115–2128.
Vallee, B.L., Auld, D.S., 1990. Zinc coordination, function, and structure of zinc enzymes and other proteins. Biochemistry 29 (24), 5647–5659.
Van Heukelem, L., Thomas, C.S., 2001. Computer-assisted high-performance liquid chromatography method development with applications to the isolation and analysis of phytoplankton pigments. J. Chromatogr. A 910 (1), 31–49.
van Leeuwe, M.A., Villerius, L.A., Roggeveld, J., Visser, R.J.W., Stefels, J., 2006. An optimized method for automated analysis of algal pigments by HPLC. Mar. Chem. 102 (3), 267–275.
van Manen, M., Tian, H.-A., Wille, F., Jung, J., Lee, Y., Lee, S.H., Kim, T.-W., Aoki, S., Eich, C., Brussaard, C., Reichart, G.-J., Gerringa, L., Conway, T.M., Middag, R., 2022. The role of the Dotson Ice Shelf and circumpolar deepwater as driver and source of dissolved and particulate iron and manganese in the Amundsen Sea polynya, Southern Ocean. Mar. Chem. 246, 104161.
Vance, D., Little, Susan H., de Souza, Gregory F., Khatiwala, S., Lohan, Maeve C., Middag, R., 2017. Silicon and zinc biogeochemical cycles coupled through the Southern Ocean. Nat. Geosci. 10 (3), 202–206.
Viljoen, J.J., Weir, I., Fietz, S., Cloete, R., Loock, J., Philibert, R., Roychoudhury, A.N., 2019. Links between the phytoplankton community composition and trace metal distribution in summer surface waters of the Atlantic Southern Ocean. Front. Mar. Sci. 6, 295.

Wåhlin, A.K., Kalén, O., Arneborg, L., Björk, G., Carvajal, G.K., Ha, H.K., Kim, T.W., Lee, S.H., Lee, J.H., Stranne, C., 2013. Variability of warm deep water inflow in a submarine trough on the Amundsen Sea shelf. J. Phys. Oceanogr. 43 (10), 2054–2070.

Weber, T., John, S., Tagliabue, A., DeVries, T., 2018. Biological uptake and reversible scavenging of zinc in the global ocean. Science 361 (6397), 72.

Wyatt, N.J., Milne, A., Woodward, E.M.S., Rees, A.P., Browning, T.J., Bouman, H.A., Worsfold, P.J., Lohan, M.C., 2014. Biogeochemical cycling of dissolved zinc along the GEOTRACES South Atlantic transect GA10 at 40°S. Glob. Biogeochem. Cycles 28 (1), 44–56.

Xie, R.C., Galer, S.J.G., Abouchami, W., Rijkenberg, M.J.A., De Jong, J., de Baar, H.J.W., Andreae, M.O., 2015. The cadmium–phosphate relationship in the western South Atlantic — the importance of mode and intermediate waters on the global systematics. Mar. Chem. 177, 110–123.

Xu, Y., Morel, F.M.M., 2013. Cadmium in marine phytoplankton. In: Sigel, Astrid, Sigel, Helmut, Sigel, R.K. (Eds.), Cadmium: from Toxicity to Essentiality. Springer, Dordrecht, pp. 509–528.

Yager, P.L., Sherrell, R.M., Stammerjohn, S.E., Alderkamp, A.-C., Schofield, O., Abrahamsen, E.P., Arrigo, K.R., Bertilsson, S., Garay, D.L., Guerrero, R., Lowry, K.E., Moksnes, P.-O., Ndungu, K., Post, A.F., Randall-Goodwin, E., Riemann, L., Severmann, S., Thatje, S., Van Dijken, G.L., Wilson, S., 2012. ASPIRE: the Amundsen Sea polynya international research expedition. Oceanography 25 (3), 40–53.

Zhao, Y., Vance, D., Abouchami, W., de Baar, H.J.W., 2014. Biogeochemical cycling of zinc and its isotopes in the Southern Ocean. Geochim. Cosmochim. Acta 125, 653–672.